



UNIVERSITY OF  
**BATH**

Department of Mechanical Engineering  
Faculty of Engineering and Design

**Final Year Dissertation**

# Design and Optimisation of a Hydrogen Peroxide Turbopump Compressor

By

Alfie James Gilmour

in partial fulfilment of the requirements for the degree of

**Master of Engineering**  
in Aerospace Engineering

at the University of Bath

*4<sup>th</sup> May 2022*

*Word Count: 11,098*

Supervisor: *Dr. Hui Tang*

Assessor: *Dr. Mauro Carnevale*

# Acknowledgments

The completion of this research could not have been possible without the expertise of Dr. Hui Tang, to whom I owe a debt of gratitude for all the advice, support and resources offered throughout my final year. Being granted the flexibility to shape this project to suit my own interests and curiosities has been invaluable to my professional development, and will ultimately stand me in good stead for a future career in academia and industry.

I would also like to thank Sean Horgan, of *80/20 Engineering Ltd.*, for all the technical support during this semester. The scope of work presented in this dissertation would not have been achievable without the use of their resources.

Lastly, I would not have succeeded without the support of my parents, Elizabeth and Mark, and my partner, Sarah. Always by my side, despite the distance.

*Alfie Gilmour*

*University of Bath, May 2022*

# Summary

Motivated by the space industry's drive for more sustainable, environmentally-clean rocket propellants, this dissertation presents a methodology framework for the preliminary development phase of a hydrogen peroxide turbopump compressor, from baseline design through to prototype proposal. The core focus was inducer, impeller, and volute development. An iterative inverse design approach was adopted to ensure each configuration was optimised for performance, with respect to a specification outlined by silver-screen catalyst bed requirements. 1D modelling tools were constructed which outputted blade angles and characteristic parameters to define initial component design points. A commercially-available turbomachinery modelling software was then used to generate practical 3D geometry. CFD simulations predicted internal flow performance, quantified by total pressure rise and efficiency, and also validated the 1D model outputs. Following three iterations, the baseline compressor produced a total pressure rise of 512 *bar* and an efficiency of 81.1%, at a shaft speed of 90,000 *rpm* and a mass flow rate of 8.00 *kg/s*. Despite this not complying with the 360 *bar* pressure rise requirement, it was proposed to run the pump at a low power mode to decrease the outlet pressure to acceptable levels. FEA studies were conducted in parallel to feedback to the design loop on load bearing and dynamic performance. Baseline results predicted total material failure, but highlighted several areas for design improvement. Modal analysis results showed no natural frequencies coincided with the pump operating window. A subsequent optimisation study was conducted to investigate the effects of splitter blades on pump performance. A clear relationship between the splitter blade leading-edge meridional position and pump efficiency was identified. This defined an optimum impeller configuration, which gave an efficiency increase of 1.6% at a splitter blade leading-edge position of 30% meridional length. A significant reduction in streamline deviation was observed within the impeller blade channels as a result. Revised inducer and impeller models fell within permissible stress and displacement limits, with a 4.8% improvement to inducer mass, although the impeller suffered an increase of 8.4% due to the addition of the splitter blades and thicker hub/shroud geometries. Ultimately, a high pressure, high efficiency, lightweight and compact compressor prototype was devised, which met all critical design requirements with slight adjustments to the nominal operating conditions.

# Table of Contents

Acknowledgments .....	i
Summary .....	ii
Table of Contents.....	iii
List of Figures .....	v
List of Tables .....	vi
List of Nomenclature and Symbols .....	vii
<b>1.0 Introduction .....</b>	<b>1</b>
1.1 Background.....	1
1.2 Research Aims and Objectives .....	2
1.3 Originality of Work .....	2
1.4 Outline of Dissertation.....	3
<b>2.0 Literature Review.....</b>	<b>4</b>
2.1 Hydrogen Peroxide as an Oxidiser .....	4
2.2 Hydrogen Peroxide Propulsion System Research .....	5
2.3 Turbopump System Overview .....	6
2.4 Compressor Stage Overview .....	7
2.4.1 Inducer.....	7
2.4.2 Impeller .....	8
2.4.3 Volute Casing.....	9
2.5 Baseline Compressor Design Parameters .....	9
<b>3.0 Purdue University Design Requirements .....</b>	<b>11</b>
3.1 Propulsion System Schematic .....	11
3.2 Design Specification Document .....	11
3.3 Hydrogen Peroxide Properties.....	11
<b>4.0 Baseline Compressor Model Development .....</b>	<b>13</b>
4.1 Iterative Design Approach.....	13
4.2 1D Model Design Tool .....	13
4.3 CFTurbo® Model Development .....	15
4.3.1 Generated 2D Meridional Geometry.....	15
4.3.2 Generated 3D Geometry.....	16
4.4 Internal Flow Analysis Setup.....	17
4.4.1 Geometry Construction.....	17
4.4.2 Simulated Fluid.....	17
4.4.3 Solver Settings.....	17
4.4.4 Boundary Conditions.....	18
4.4.5 Mesh Construction and Independence Study .....	18
4.5 Structural Analysis Setup.....	21
4.5.1 Geometry Construction.....	21
4.5.2 Simulated Loads and Supports.....	21
4.5.3 Material Selection.....	22
4.5.4 Element Sensitivity Study .....	22
4.5.5 Mesh Independence Study .....	23
4.5.6 Generated Meshes.....	24
4.5.7 Modal Analysis Setup .....	25
<b>5.0 Simulated Flow Performance .....</b>	<b>26</b>
5.1 Design Iterations.....	26
5.2 Baseline Compressor Performance .....	27
<b>6.0 Simulated Structural Performance .....</b>	<b>29</b>
6.1 Static Load Performance .....	29
6.2 Dynamic Behaviour.....	31

<b>7.0</b>	<b>Optimisation Study .....</b>	<b>32</b>
<b>7.1</b>	<b>Splitter Blade Integration .....</b>	<b>32</b>
<b>7.2</b>	<b>Structural Improvements .....</b>	<b>34</b>
7.2.1	<i>Component Modifications.....</i>	<i>34</i>
7.2.2	<i>Revised Structural Performance.....</i>	<i>35</i>
7.2.3	<i>Revised Dynamic Performance.....</i>	<i>36</i>
7.2.4	<i>Mass Characteristics.....</i>	<i>36</i>
<b>8.0</b>	<b>Proposed Compressor Prototype .....</b>	<b>37</b>
<b>8.1</b>	<b>Inducer.....</b>	<b>37</b>
<b>8.2</b>	<b>Impeller .....</b>	<b>38</b>
<b>8.3</b>	<b>Volute .....</b>	<b>39</b>
<b>9.0</b>	<b>Conclusions and Recommendations .....</b>	<b>40</b>
<b>9.1</b>	<b>Conclusions .....</b>	<b>40</b>
<b>9.2</b>	<b>Recommendations for Future Work.....</b>	<b>40</b>
<b>10.0</b>	<b>References .....</b>	<b>41</b>
<b>10.1</b>	<b>Literature.....</b>	<b>41</b>
<b>10.2</b>	<b>Figures.....</b>	<b>43</b>
<b>11.0</b>	<b>Appendices .....</b>	<b>44</b>
<b>11.1</b>	<b>Appendix A – 1D Model Code .....</b>	<b>44</b>
<b>11.2</b>	<b>Appendix B – Inducer Technical Drawing.....</b>	<b>50</b>
<b>11.3</b>	<b>Appendix C – Impeller Technical Drawing .....</b>	<b>51</b>

# List of Figures

<b>Figure 1:</b> Catalytic, exothermic decomposition mechanism of HTP [A].	5
<b>Figure 2:</b> Turbopump cutaway views depicting component form and layout [B,C].	6
<b>Figure 3:</b> Labelled sketch of axial inducer [D].	7
<b>Figure 4:</b> Labelled sketch of shrouded impeller [D].	8
<b>Figure 5:</b> Splitter blade length in comparison to main blade length. Respective LEs are fixed [E].	8
<b>Figure 6:</b> Labelled sketch of volute casing [D].	9
<b>Figure 7:</b> Engine system flow schematic based on the PU configuration [D].	11
<b>Figure 8:</b> HTP compressor design requirements derived from the PU publications [3,4,15,17].	12
<b>Figure 9:</b> Iterative inverse design process for the HTP compressor. Adapted from [F].	13
<b>Figure 10:</b> Velocity triangles used as the basis for the 1D preliminary compressor model [G].	13
<b>Figure 11:</b> Compressor subassembly meridional view. Dimensions are included for reference.	15
<b>Figure 12:</b> Respective Cordier plots for the inducer and impeller.	16
<b>Figure 13:</b> View of generated 3D compressor geometry from Cfturbo®.	16
<b>Figure 14:</b> Component flow domains. A section view of the inducer has been used for reference.	17
<b>Figure 15:</b> Prescribed boundary conditions (BCs) for the compressor model.	18
<b>Figure 16:</b> Mesh convergence study concerning the total pressure rise against element count. A 0.1% error band has been included for reference.	19
<b>Figure 17:</b> Generated component meshes using Setting 4.	20
<b>Figure 18:</b> Overview of the baseline geometry used for the initial static analyses.	21
<b>Figure 19:</b> Established load cases for the baseline static analyses.	21
<b>Figure 20:</b> Component BCs on respective hubs.	22
<b>Figure 21:</b> Mesh convergence studies showing stress variation with node count.	23
<b>Figure 22:</b> Generated component meshes and topology refinement regions at respective LEs.	24
<b>Figure 23:</b> Aspect Ratio distribution for both generated meshes.	24
<b>Figure 24:</b> Total pressure contour plots and velocity streamlines at the impeller mid-section.	26
<b>Figure 25:</b> Total pressure contour plots at the impeller mid-section.	28
<b>Figure 26:</b> Compressor performance map for three speed modes. Results have been normalised by the design points of 360 bar and 8.00 kg/s.	28
<b>Figure 27:</b> Impeller static load results depicting endured stresses.	29
<b>Figure 28:</b> Impeller static load results depicting global displacement.	29
<b>Figure 29:</b> Inducer static load results depicting endured stresses.	30
<b>Figure 30:</b> Inducer static load results depicting global displacement.	30
<b>Figure 31:</b> Derived natural frequencies for both components, depicting each mode pair.	31
<b>Figure 32:</b> Comparison of impeller standard and splitter blade designs.	32
<b>Figure 33:</b> Variation of efficiency with LE position.	33
<b>Figure 34:</b> Revised compressor performance map.	33
<b>Figure 35:</b> Comparison of streamline congruence in standard and splitter blade impeller configurations.	33
<b>Figure 36:</b> Inducer structural modification summary.	34
<b>Figure 37:</b> Impeller structural modification summary.	34
<b>Figure 38:</b> Revised impeller structural performance. A deformation factor of 270 is applied to (b).	35
<b>Figure 39:</b> Revised inducer structural performance.	35
<b>Figure 40:</b> Inducer velocity triangles as derived from the 1D model.	37
<b>Figure 41:</b> Impeller velocity triangles as derived from the 1D model.	38
<b>Figure 42:</b> Design summary of the volute, derived from outputs of the 1D model.	39

# List of Tables

<b>Table 1:</b> Properties of 90% concentration hydrogen peroxide at 298K.....	11
<b>Table 2:</b> 1D model code structure – script inputs and outputs.....	14
<b>Table 3:</b> Mesh characteristics for each quality setting. ....	18
<b>Table 4:</b> Global average Y+ values. ....	19
<b>Table 5:</b> Summary of PS and SS pressure values to construct the blade loading condition. ....	21
<b>Table 6:</b> Inconel 178 isotropic material specification for CFTurbo FEA®.....	22
<b>Table 7:</b> Inducer element sensitivity study results. ....	23
<b>Table 8:</b> Impeller element sensitivity study results.....	23
<b>Table 9:</b> Inducer and impeller mesh summaries.....	24
<b>Table 10:</b> Result summary for each design iteration. ....	26
<b>Table 11:</b> Characteristic pump performance for nominal and off-design conditions. ....	27
<b>Table 12:</b> Baseline compressor natural frequencies. ....	31
<b>Table 13:</b> SS 17-4 PH isotropic material specification for CFTurbo FEA®.....	34
<b>Table 14:</b> Revised component natural frequencies. ....	36
<b>Table 15:</b> Comparison of baseline and optimised component mass characteristics. ....	36
<b>Table 16:</b> Final inducer characteristics. ....	37
<b>Table 17:</b> Inducer blade angles. ....	37
<b>Table 18:</b> Final impeller characteristics.....	38
<b>Table 19:</b> Impeller blade angles.....	38

# List of Nomenclature and Symbols

## Nomenclature

CAD	Computer Aided Design
CFD	Computational Fluid Dynamics
CNSA	China National Space Administration
ESA	European Space Agency
FEA	Finite Element Analysis
HTP	High-test Peroxide
ISS	International Space Station
NASA	National Aeronautics and Space Administration
PU	Purdue University
RATO	Rocket-assisted Take-off
RP-1	Highly refined form of kerosene
ULA	United Launch Alliance

## Symbols

$A$	Area [ $m^2$ ]	$\alpha$	Thermal Expansion Coefficient [ $K^{-1}$ ]
$C$	Absolute Velocity [ $m/s$ ]	$\beta$	Flow Angle [ $^\circ$ ]
$c_p$	Specific Heat Capacity [ $Jkg^{-1}K^{-1}$ ]	$\delta$	Specific Diameter [-]
$E$	Young's Modulus [ $GPa$ ]	$\Delta P_{TOT}$	Total Pressure Rise [ $bar$ ]
$F$	Thrust [ $N$ ]	$\Delta V$	Velocity Increment [ $m/s$ ]
$g_0$	Gravitational Constant [ $m/s^2$ ]	$\eta$	Efficiency [-]
$H_T$	Total Pump Head [ $m$ ]	$k$	Thermal Conductivity [ $Wm^{-1}K^{-1}$ ]
$I_{sp}$	Specific Impulse [ $s$ ]	$\lambda$	Weighted Parameter [-]
$M$	Torque [ $Nm$ ]	$\nu$	Kinematic Viscosity [ $m^2/s$ ]
$M_{HP}$	HTP Molar Mass [ $gmol^{-1}$ ]	$\nu_{PR}$	Poisson's Ratio [-]
$m_p$	Propellant Mass [ $kg$ ]	$\rho$	Density [ $kgm^{-3}$ ]
$NPSH$	Net Positive Suction Head [ $m$ ]	$\sigma$	Specific Speed [-]
$P$	Total Pressure [ $bar$ ]	$\sigma_{UTS}$	Ultimate Tensile Strength [ $MPa$ ]
$p$	Static Pressure [ $Pa$ ]	$\sigma_Y$	Yield Strength [ $MPa$ ]
$P_{required}$	Required Power [ $W$ ]	$\varphi$	Flow Coefficient [-]
$Q$	Flow rate [ $m^3/s$ ]	$\psi$	Work Coefficient [-]
$r$	Radius [ $m$ ]	$\omega$	Angular Speed [ $rad/s$ ]
$t$	Time [ $s$ ]		
$U$	Tangential Velocity [ $m/s$ ]		

## Subscripts

1	Station 1
2	Station 2
$A$	Available
$b$	Blade
$C$	Absolute
$in$	Inlet
$m$	Meridional
$mat$	Material
$out$	Outlet
$R$	Required
$tip$	Component tip
$u$	Tangential
$v$	Vapour
$W$	Relative



# 1.0 Introduction

## 1.1 Background

Liquid rocket propulsion is an integral part of the modern space industry. Notable launch vehicles such as the SpaceX *Falcon 9*, CNSA *Long March 8*, ESA *Ariane 5*, and ULA *Atlas V* all utilise liquid rocket engine systems, alone, or in combination with solid boosters to conduct a variety of missions – from ISS transportation to satellite delivery [1]. This is because of their notable efficiency, versatility and, more recently, reusability. The former is commonly quantified as the Specific Impulse,  $I_{sp}$ , which is a measure of the thrust produced per unit rate of propellant consumption, namely,

$$I_{sp} = \frac{\int F dt}{g_0 m_p}. \quad (1)$$

Engine  $I_{sp}$  is critical to achieving a certain velocity increment  $\Delta V$  based on mission requirements, which defines the launch and manoeuvre capabilities of the spacecraft [2]. Improving the  $I_{sp}$  of a given propulsion system can be achieved by adopting higher chamber pressures. However, for pressure-fed engines, this requires higher propellant tank pressure, which in turn requires stronger tanks at the expense of increased mass. Therefore, it is conventional to utilise turbopump systems in high-thrust engines to meet the demanding chamber pressures and propellant flow rates. A turbopump assembly comprises a compressor driven by a turbine at high rotational speeds, which impels the propellant into the combustion chamber. Hence, it is obvious that engine requirements are closely coupled with the turbopump system design, such that improving turbopump operation can help drive the maximum obtainable  $I_{sp}$  and combustion efficiency.

In light of more sustainable propulsion, environmentally-clean rocket propellants are a key driver in assuring the future of space travel, especially for the feasibility of commercial orbital launches and beyond. Rocket grade hydrogen peroxide (HTP) was typically reserved for limited performance applications due to pressure-fed propellants or low-performance turbopump cycles. However, in the last decade, interest has been rekindled into its use in the next generation of liquid rocket engines due to its low toxicity, clean combustion products, and attainable  $I_{sp}$ . Thus, the presented work aims to initiate the development of a high pressure, lightweight and compact turbopump system for use with HTP and RP-1 fuel. The ultimate goal is to achieve an efficient configuration that promotes the benefits of adopting the propellant.

## **1.2 Research Aims and Objectives**

The aim of this project is to oversee the design phase of an HTP/RP-1 turbopump oxidiser compressor, from baseline design through to prototype proposal. This will include an iterative inverse design approach to ensure the configuration is optimised for performance, with respect to a pre-defined requirements specification. To achieve the overarching aim of this project, the identified objectives are:

1. To establish a comprehensive design specification for the compressor, defined by the turbopump use-case, and define the compressor operating window.
2. To construct 1D modelling tools to achieve initial component geometry and automate the design workflow.
3. To use CAD modelling software to generate geometry which is compatible with chosen CFD and FEA software packages.
4. To conduct CFD simulations to determine flow performance, such as total pressure rise and efficiency, and validate the 1D models in N°2.
5. To conduct FEA simulations to predict structural and dynamic performance, and to provide optimisation feedback.
6. To iterate the model to converge on a refined solution which complies with the design specification.
7. To oversee an optimisation study where a splitter blade configuration will be investigated to evaluate the influence on pump performance.
8. To construct a final design package ready for manufacture. This will include technical drawings and component specifications.

## **1.3 Originality of Work**

The presented literature review in this dissertation highlights the limited research on HTP turbomachinery. In addition, while several academic groups invest into the research of turbopump components, only a select number possess the capabilities for the entire design and production of turbopump assemblies. Hence, the number of studies conducted on HTP turbopump compressors is highly contained, with only one notable institution, Purdue University, publishing a series of design reports on HTP turbomachinery development, which only provide broad overviews of relevant methodologies.

Therefore, the novelty introduced by this research lies in:

1. A more in-depth methodology framework for the baseline design of HTP turbopump compressors.
2. The application of CFD-based optimisation by investigating the effects of splitter blades on HTP compressor performance.
3. The delivery of FEA-based optimisation of HTP inducer and impeller geometries in parallel with flow performance predictions.

## 1.4 Outline of Dissertation

This dissertation summarises the most important aspects of the conducted research. The intention is to provide an in-depth account of the methodology framework to offer reproducibility of the baseline design and optimisation of the HTP compressor.

The following layout is presented:

**Chapter 2** provides a critique of relevant literature surrounding HTP capabilities and turbopump component design. Theoretical concepts are presented to provide additional context.

**Chapter 3** presents all propulsion system and design specifications which will drive compressor development.

**Chapter 4** outlines all methodologies used to develop a baseline compressor model.

**Chapter 5** summarises all key results which depict the internal flow performance of the baseline compressor.

**Chapter 6** summarises all key results which depict the structural and dynamic behaviour of the baseline compressor.

**Chapter 7** provides a further optimisation study where splitter blades integration is investigated, as well as a summary of structural optimisation work.

**Chapter 8** outlines all design summaries which define the compressor componentry.

**Chapter 9** presents the conclusions and recommendations for further study.

## 2.0 Literature Review

### 2.1 Hydrogen Peroxide as an Oxidiser

Since the 1950s, rocket engines which utilise HTP as a liquid oxidiser or monopropellant have predominantly been used for low performance applications, such as RATO or sub-orbital sounding rockets. Typically, these engines function at low chamber pressures using pressure-fed propellants, open-cycle turbopumps, or low-pressure closed-cycle turbo-pumps. As a result, HTP rocket engines have generally exhibited limited performance compared to other engine architectures [3,4]. However, in the last decade, interest into the use of HTP has grown, specifically for bipropellant engines which utilise both a fuel and an oxidiser to achieve combustion [5]. This shift is attributed to the focus on sustainable engine development, with low-toxicity, storable liquid propellants becoming more attractive as substitutes for conventional oxidisers [6].

HTP follows liquid oxygen as the most effective oxidiser and possesses several properties which make it a desirable choice in the next generation of rocket propulsion. HTP is non-toxic and, depending on the engine configuration, produces clean combustion products. This makes it far more desirable than oxidisers which are toxic in manufacture and combustion, such as oxides of nitrogen and hydrazines [7,8]. Performance predictions from G.P.Sutton et. al. demonstrated that, when coupled with RP-1 fuel, HTP provides an acceptable  $I_{sp}$  of 319 seconds compared to using liquid oxygen which yields 360 seconds [9]. Despite this decrease in performance, A.Cervone et. al. argue that HTP avoids the investment and complexity of cryogenic storage, which is required by liquid oxygen and hydrogen, where a range of tank pressurisation gases can also be used [10]. This highlights the versatility of HTP in space operations, and the motivation for this research.

Contrarily, various properties of HTP have led to criticisms concerning its use as a future oxidiser, with the most notable being J.Clark's 1972 seminal work [11]. This provides a comprehensive critique of HTP, and his polemic against using the propellant, loosely paraphrased as *"... always the bridesmaid; never the bride"*, generated a high degree of bias amongst the rocket community for decades [11,12]. However, in the light of present experience and knowledge, J.Clark's assessment was criticised by A.J.Musker et. al. in hopes of rekindling interest in HTP [12]. The arguments and respective counterarguments are presented in order of importance.

Firstly, J.Clark highlighted the detonation risk posed by stored HTP, which will exothermically decompose if contact is made with certain propellants. However, in the context of liquid rocket propulsion, it is routine practice to keep the fuel and oxidiser completely separated during ground operations [12]. Concerns were also raised about the contamination risk and storage stability of the oxidiser. Although, significant improvements in manufacturing and storage capabilities have since led to increased safety of HTP through the addition of stabilising agents and advancements in storage materials [12,13]. Finally, it was proposed that HTP's higher freezing point could restrict its use in missions which involve limited exposure to the Sun [12]. However, the storage of HTP in cold climates is well documented, and confirms its low tendency to freeze due to its super-cooling properties [12].

Overall, there is an apparent enthusiasm in recent publications which affirms the benefits of adopting HTP in the next generation of sustainable liquid rocket engines. Hence, a key driver for this project is to further this development by harnessing the, previously misrepresented, capabilities of hydrogen peroxide.

## 2.2 Hydrogen Peroxide Propulsion System Research

There are two HTP ignition method used in bipropellant engines. Hypergolic ignition utilises HTP in conjunction with a fuel and catalyst mixture to trigger combustion. Autoignition, however, utilises HTP decomposition over a catalyst bed to produce superheated oxygen and water vapour. This is ultimately used to drive a turbine, as part of a turbopump subassembly, and routed into a combustion chamber to oxidise and combust a fuel [5,14,15]. This research will focus on the latter method. The HTP decomposition mechanism is illustrated in Figure 1.

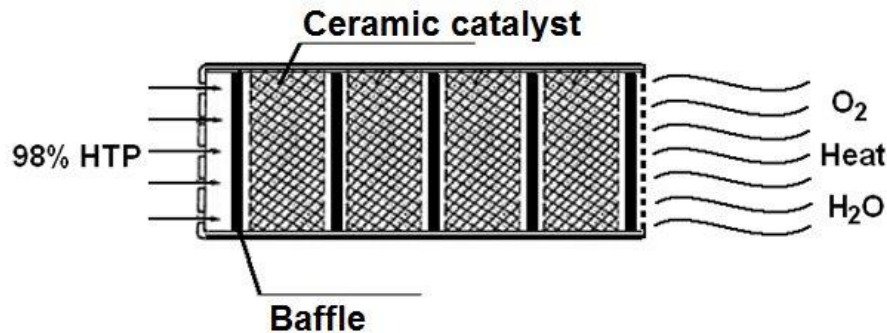


*Figure 1: Catalytic, exothermic decomposition mechanism of HTP [A].*

Recent advances in high-pressure silver screen catalyst bed design at Purdue University's Zucrow Research Laboratories proved operation at "much higher bed loadings and pressures than previously believed" [3,4]. Thus, by leveraging modern technology, it has been possible to significantly improve HTP engine performance by utilising closed-cycle systems at higher chamber pressures than what was previously possible. This has allowed for higher specific impulses, low masses, and smaller components to be achieved [4]. These developments have granted Purdue University (PU) significant reputation at the forefront of HTP rocket engine R&D, and their published work, namely those which cover turbopump design, are of great importance to this project.

M.Ventura et. al. provided a feasibility study on the modern usage of HTP, which highlights the main difficulties faced when adopting the oxidiser. While this lacked an in-depth technical appraisal, it provided a sound basis for the followed design work at PU, and additional context for this project [16]. A development cycle overseen by W.L.Murray et. al., covering the design and analysis of a complete HTP/RP-1 turbopump assembly, provides an overview of the required methodologies and baseline theory to follow the development [3]. The publication presents all relevant stages of the design phase, including the requirements specification, initial design construction, CFD analysis, and hardware design and manufacture. Despite providing a broad overview of the project, the paper lacks specific details of geometry and analysis settings for complete reproducibility. This was complemented by a subsequent paper, which focussed on manufacture and testing of a functional turbopump prototype of the same design [17]. This offered more insight into the practical implications of certain design decisions, as well as the design of turbopump ancillaries not previously covered. However, besides content relating to manufacture, the paper did not provide additional material on HTP compressor design. Thus, the research presented in this dissertation aims to expand on this contained area of turbomachinery design.

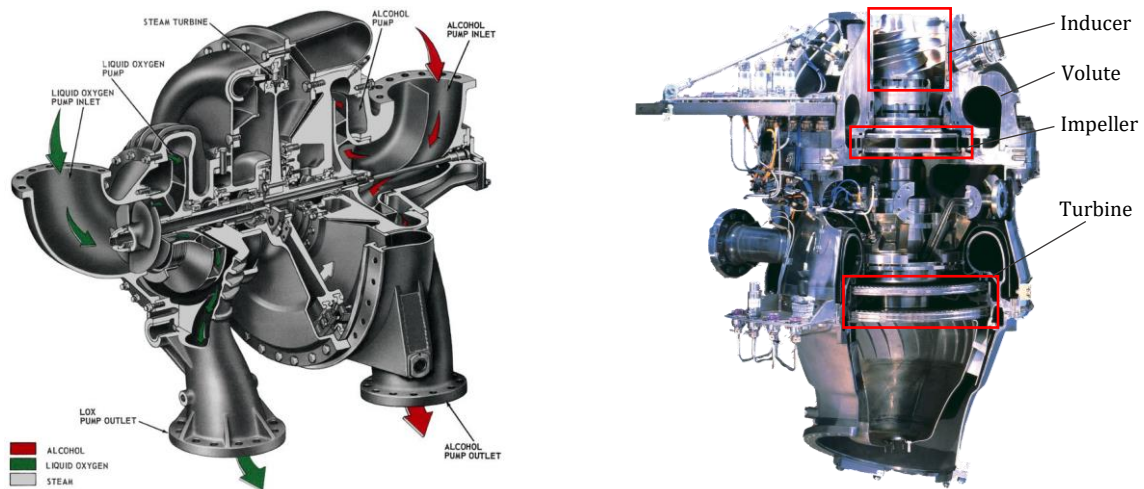
Publications outside of PU which focus on the design of HTP turbomachinery are limited. Furthermore, while many academic research groups investigate and optimise turbopump components extensively, only a select number of bodies possess the knowledge and capabilities for the entire design and eventual production of turbopumps for liquid rocket engines [17]. Hence, the series of publications from PU provide a cohesive methodological framework which will form the foundation of this project.

As summarised, an opportunity has been identified to utilise modern engineering capabilities to contribute to the development of a high speed, high pressure HTP/RP-1 turbopump prototype which feeds a silver screen catalyst bed, the specification of which being outlined by PU [3]. This will act as a proof of concept for the next generation of high performance HTP turbopumps, in the light of more efficient, sustainable rocket propulsion.

## 2.3 Turbopump System Overview

Several turbopump configurations are possible, but at its core, it consists of two key elements: a hot gas-powered turbine, and one or two propellant pumps designated for the fuel and oxidiser, which are driven by the turbine. The pump, or compressor, is usually divided into three components: the inducer, the impeller, and the volute [1]. Component layout and working fluid flow is illustrated in Figure 2.

The turbopump forms an integral part of the overall propulsion system architecture, and its operational requirements are closely coupled to the engine requirements, which are ultimately defined by the vehicle mission profile [18]. In bipropellant engines, it bridges the propellant main tanks and thrust chamber, and its purpose is to increase the pressure of the oxidiser and fuel prior to combustion [18,19]. It is a high-precision rotary machine which operates at high shaft speed, whilst handling extreme thermal gradients and pressure variations [19]. Thus, it is acknowledged that turbopumps operate close to the limits of what is possible with current technology, and the ever-increasing demand for higher chamber pressures and efficiencies has truly tested the capabilities of rocket turbomachinery design.



(a) Redstone A-7 turbopump cutaway diagram.

(b) Vulcain 2 turbopump cutaway.

**Figure 2:** Turbopump cutaway views depicting component form and layout [B,C].

A review of the literature surrounding turbopump development has highlighted extensive research into the design and analysis of individual components. Although, excluding the PU publications, a lack of diversity is present in research which covers complete system development. The main documentation which bridges this gap is the NASA Design Criteria [20,21,22]. These provide a coherent and comprehensive overview of all required design steps, and are laden with theoretical and empirical methods which are of use to this project. However, many of these reports are outdated, and do not address the vast improvements made to the design methods and techniques since the 1970s.

## 2.4 Compressor Stage Overview

### 2.4.1 Inducer

The inducer is located on the axial inlet portion of the compressor, as depicted in Figure 2b. It is situated upstream of the impeller and its functions are to raise the static pressure by an amount sufficient to avoid cavitation on the highly-loaded impeller blades, improve suction performance, and reduce tank pressure and mass [1,20]. This study concerns a configuration where the inducer is coupled to the impeller by a central drive shaft [20]. Figure 3 illustrates a diagrammatic sketch of an inducer.

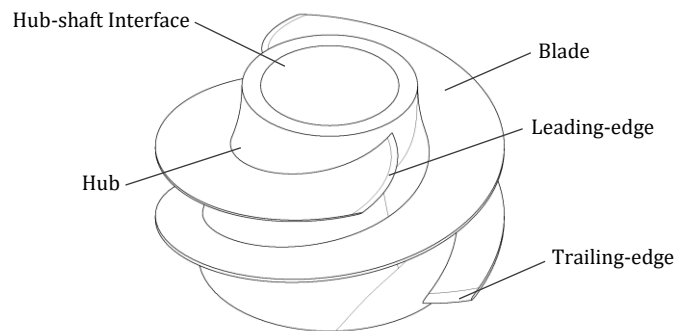


**Figure 3:** Labelled sketch of an axial inducer [D].

Cavitation is a pressure-driven phase change which occurs in a local region of the flow where the static pressure drops below the fluid vapour pressure [1]. This generates a vapour-filled cavity so that a two-phase flow is created in a small domain of the flow field. Instabilities due to the unsteadiness of cavitation induce streamline deviation which, in turn, leads to uneven blade loading, mechanical stresses and vibrations [1,23]. In the context of turbopump compressors, cavitation mainly occurs across the inducer blade suction side. Thus, inducers typically utilise sharp leading edge and thin blades, designed to work at little incidence angles in order to preclude cavitation [23].

Inducer design is primarily focused on achieving a sufficient cavitation margin instead of maximising efficiency. Thus, contrary to impeller design, inducers typically have lower flow coefficients and inlet angles, higher blade solidities, and fewer blades [24]. As reported in the NASA Design Criteria, inducer design is limited by structural constraints, because of permissible blade root stresses, flow instabilities, and centrifugal loads [20]. Thus, an optimal design provides a sound compromise between suction and structural performance [21].

In literature, inducer design and analysis is well covered. S-S.Hong et. al. conducted computational and experimental studies on inducer performance for liquid rocket engine applications. This confirmed inducers have negligible effects on the pump head and efficiency, but a significant influence on cavitation performance [25]. D.Japikse provided an overview of current practices which offer guidance on high-performance inducer design [26]. Few papers cover the baseline design of inducers in terms of 1D modelling techniques. Although, M.Mohr provided an in-depth appraisal of the relevant procedures [27]. Overall, a wide range of sources are available to aid with the research presented in this dissertation.

### 2.4.2 Impeller

The centrifugal impeller section, downstream of the inducer, converts most of the shaft power into pressure rise and kinetic energy of the pumped fluid prior to combustion [21]. Impeller types include fully shrouded, open faced, or completely unshrouded configurations. This study will utilise a shrouded impeller design to minimise tip leakage flows and ensure blade integrity is maintained [3,21]. Figure 4 presents all important features of a shrouded impeller.

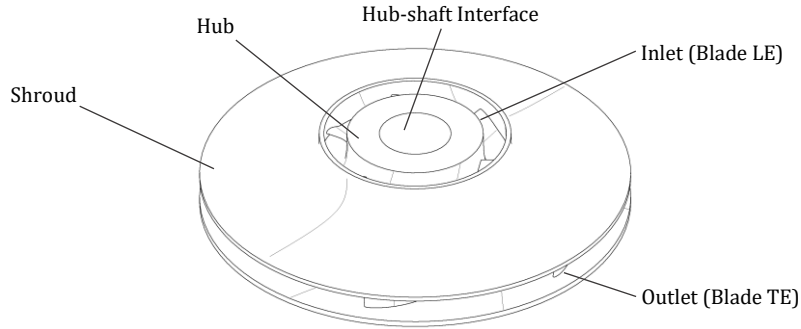


**Figure 4:** Labelled sketch of a shrouded impeller [D].

Impeller design methods and performance predictions are well established in literature. Baseline modelling is clearly outlined by J.T.Gravdahl et. al., which will help the 1D model construction phase of this research [28]. M.D.Mentzos et al. utilised CFD simulations to predict flow behaviour across the impeller domain. This offered insight into the computational methodologies used to assess performance [29]. Finally, A.S.Prasad et. al. conducted static and dynamic analyses on a centrifugal impeller, which highlighted the importance of monitoring the structural behaviour during the early design phase [30].

Several features can be included in impeller designs to improve flow performance. One notable addition is splitter blades. As illustrated in Figure 5, these are blades of reduced length, with the leading edge shifted downstream of the impeller inlet [1]. These have been reported to reduce blockage at the impeller inlet by effectively decreasing blade channel area. Reduced blockage corresponds to lower velocities, higher pressures and, hence, increased cavitation performance [1]. This mechanism was confirmed by D.Japkise et. al. and R.B.Furst [31,32]. Furthermore, splitter blades have been reported to promote improved streamline adherence by reducing deviation through impeller channels. This results in more uniform blade loading, and decreased mechanical stresses and vibrations [33]. A splitter blade mean line optimisation framework was presented by F.Torre et. al., which demonstrated the true potential of splitter blades in liquid rocket turbopumps. By leveraging the full flexibility of splitter blade design, significant cavitation and pump operating range improvements were achieved [33]. There are no records of splitter blade research concerning HTP-based turbopump impellers. Therefore, a gap in this area of rocket turbomachinery literature has been identified, which this dissertation aims to address.

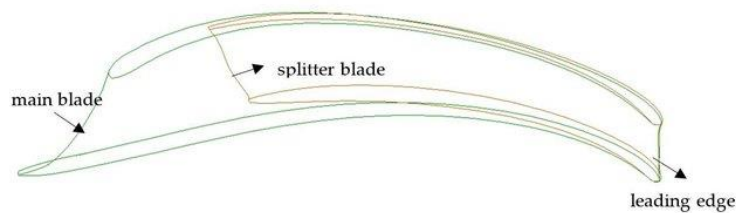


**Figure 5:** Splitter blade length in comparison to main blade length. Respective LEs are fixed [E].



### 2.4.3 Volute Casing

The final component which is of importance to this project is the volute casing. Its purpose is to collect the working fluid after leaving the impeller. As the fluid travels along the spiral, additional mass flow is added from the impeller exit. Due to an increasing cross-sectional area with circumferential angle, the velocity is maintained. This results in a uniform pressure distribution across this stage [9]. A diagram of the volute casing is shown in Figure 6. Limited publications are present on performance assessments of turbopump volute casings, as they typically form part of much broader investigations.

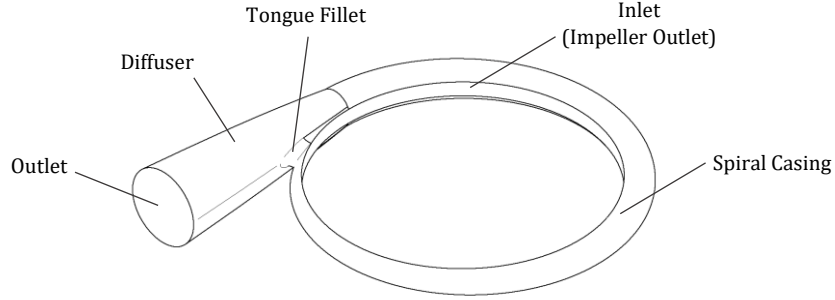


**Figure 6:** Labelled sketch of a volute casing [D].

## 2.5 Baseline Compressor Design Parameters

This section aims to introduce the underlying pump performance theory used to construct the baseline 1D models. The total pressure rise,  $\Delta P_{TOT}$ , across the compressor can be expressed as the total head,

$$H_T = \frac{\Delta P_{TOT}}{\rho g_0} = \frac{P_{out} - P_{in}}{\rho g_0}. \quad (2)$$

It is convenient to express the total in non-dimensional form. The work coefficient is defined,

$$\psi = \frac{P_{out} - P_{in}}{\rho u_2^2} = \frac{P_{out} - P_{in}}{\rho r_2^2 \omega^2}, \quad (3)$$

where the  $u_2$  is the circumferential velocity at the impeller outlet. Thus, the work coefficient is a characteristic parameter of the impeller. Similarly, the flow coefficient for the inducer can be written,

$$\varphi = \frac{c_{m,in}}{u_{tip}} = \frac{Q}{A_2 r_2 \omega}, \quad (4)$$

where  $c_{m,in}$  and  $u_{tip}$  represent the meridional absolute velocity component and tangential velocity at the inducer tip, respectively. The flow coefficient is defined at the inducer section of the compressor as it is a useful parameter for quantifying cavitation performance [23]. Inducer and impeller specific diameter,  $\delta$ , and specific speed,  $\sigma$ , can now be presented empirically [34],

$$\delta = \frac{\psi^{1/4}}{\varphi^{1/2}}, \quad (5)$$

$$\sigma = \frac{\varphi^{1/2}}{\psi^{3/4}}. \quad (6)$$

The onset of cavitation occurs when the available net positive suction head,  $NPSH_A$ , falls below the required net positive suction head,  $NPSH_R$  [3]. These are defined by Equations 7 and 8, respectively,

$$NPSH_A = \left( \frac{p_{in}}{\rho g} + \frac{C^2}{2g} \right) - \frac{p_v}{\rho g}, \quad (7)$$

$$NPSH_R = \lambda_c \left( \frac{C^2}{2g} \right) + \lambda_w \left( \frac{W^2}{2g} \right), \quad (8a)$$

$$\lambda_c = 1.15, \quad (8b)$$

$$\lambda_w = 0.20. \quad (8c)$$

Assuming inviscid, incompressible flow, the relationship between work and flow coefficients can be derived by applying the Bernoulli equation for a rotating system [1]. Between inlet and outlet stations 1 and 2, respectively,

$$P_2 - P_1 = \rho\omega(c_{2u}r_2 - c_{1u}r_1). \quad (9)$$

By also assuming zero pre-swirl at the inducer inlet,  $c_{1u} = 0$ , and utilising Equation 3 and Equation 4, the relationship between  $\psi$  and  $\varphi$  can be defined,

$$\psi = 1 - \varphi \cot \beta_2. \quad (10)$$

Similarly, the external torque,  $M$ , on the system can be expressed as,

$$M = \rho Q(c_{2u}r_2 - c_{1u}r_1). \quad (11)$$

By the definition of power in terms of angular velocity, the required power for the system is derived,

$$P_{required} = M\omega = \rho Q(c_{2u}u_2 - c_{1u}u_1). \quad (12)$$

### 3.0 Purdue University Design Requirements

#### 3.1 Propulsion System Schematic

The ultimate objective is for the oxidiser compressor assembly to be integrated within a launcher for a low-orbit micro-satellite [3]. As part of a design study by PU, a full propulsion system schematic was presented for such an application, and this will be a key driver to formulate the compressor design specification. The schematic is provided in Figure 7.

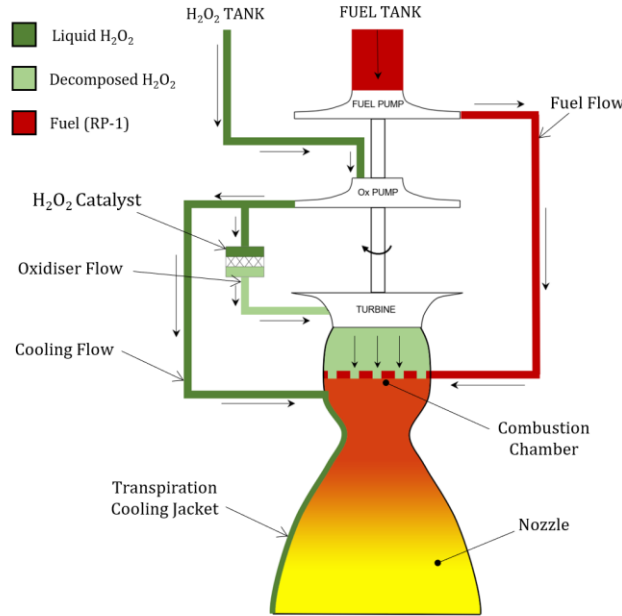


**Figure 7:** Engine system flow schematic based on the PU configuration [D].

The nominal operating point for the compressor included a mass flow rate of  $8.00 \text{ kg/s}$ , a required total pressure difference of  $360 \text{ bar}$ , a shaft speed of  $90,000 \text{ rpm}$ , and an inlet stagnation pressure of  $4.15 \text{ bar}$  and temperature of  $298 \text{ K}$ .

#### 3.2 Design Specification Document

Derived from the requirements outlined by the PU publications, a design specification document was constructed to summarise all criteria which the compressor prototype should satisfy. This was routinely interrogated and revised throughout the project to ensure both configuration control and system compliance. The final revision is provided in Figure 8.

#### 3.3 Hydrogen Peroxide Properties

The physical and chemical properties of 90% concentration HTP at  $298 \text{ K}$  were obtained from the Knovel® Engineering Technical Reference database [35,36]. These are given in Table 1.

**Table 1:** Properties of 90% concentration hydrogen peroxide at  $298 \text{ K}$ .

Property	Value	Units
Density, $\rho$	1400	$\text{kgm}^{-3}$
Kinematic Viscosity, $\nu$	$8.27 \times 10^{-7}$	$\text{m}^2\text{s}^{-1}$
Thermal Conductivity, $k$	588	$\text{Wm}^{-1}\text{K}^{-1}$
Heat Capacity, $c_p$	2774	$\text{Jkg}^{-1}\text{K}^{-1}$
Vapour Pressure, $p_v$	434	$\text{Pa}$
Molar Mass, $M_{HP}$	34.01	$\text{gmol}^{-1}$

ID	DATE	SOURCE	ITEM	TARGET	PRIORITY
<b>1.0</b>	<b>OVERALL SYSTEM REQUIREMENTS</b>				
1.1	07/02/2022	Purdue University	Working fluid	90% Concentration HTP	High
1.2	07/02/2022	Purdue University	Total Pressure Rise	360 bar	High
1.3	07/02/2022	Purdue University	Inlet Total Pressure	4.15 bar	Medium
1.4	07/02/2022	Purdue University	Working Temperature	298K	Medium
1.5	07/02/2022	Purdue University	Nominal Design Speed	90,000 rpm	Medium
1.6	07/02/2022	Purdue University	Nominal Mass Flow Rate	8.00 kg/s	High
1.7	07/02/2022	Purdue University	Redline Design Speed	100,000 rpm	Low
1.8	07/02/2022	Purdue University	Redline Mass Flow Rate	8.90 kg/s	Low
1.9	07/02/2022	Purdue University	Low Power Design Speed	75,000 rpm	High
1.10	07/02/2022	Purdue University	Low Power Mass Flow Rate	6.50 kg/s	High
<b>2.0</b>	<b>INDUCER REQUIREMENTS</b>				
2.1	07/02/2022	Purdue University	Impeller Cavitation Loss	Less than 3% total pump head	Medium
2.2	07/02/2022	Purdue University	Inlet Diameter	Greater than shaft diameter	High
2.3	07/02/2022	Purdue University	Outlet hub diameter	Equal to impeller inlet hub diameter	High
2.4	07/02/2022	Purdue University	Tip diameter	Equal to impeller inlet tip diameter	High
2.5	07/02/2022	Purdue University	Tip clearance	0.10 mm	Medium
2.6	07/02/2022	Purdue University	Suction specific speed	Maximise	Medium
2.7	07/02/2022	Purdue University	Flow Coefficient	0.10	High
2.8	07/02/2022	Purdue University	Generated head (Energy fraction)	6% of total pump head	Medium
2.9	07/02/2022	Purdue University	Slip Tolerance (Deviation)	<15°	Low
2.10	07/02/2022	Purdue University	Efficiency	>70%	Medium
2.11	14/02/2022	Design Brief	Compactness	Less than 15mm in length	Medium
<b>3.0</b>	<b>IMPELLER REQUIREMENTS</b>				
3.1	07/02/2022	Purdue University	Outer Diameter	<65 mm	Medium
3.2	07/02/2022	Purdue University	Efficiency	>60%	Medium
3.3	14/02/2022	Design Brief	Impeller Type	Shrouded	High
<b>4.0</b>	<b>STRUCTURAL REQUIREMENTS</b>				
4.1	14/02/2022	Design Brief	Design Stress	85% of yield stress	High
4.2	14/02/2022	Design Brief	Structural efficiency	Maximise	Medium
4.3	14/02/2022	Design Brief	Fatigue Life	Maximise	Medium
4.4	01/03/2022	Design Meeting	Natural Frequencies	Outside operating window	High
4.5	01/03/2022	Design Meeting	Component Inertia	Minimise	Medium

*Figure 8: HTP compressor design requirements derived from the PU publications [3,4,15,17].*

## 4.0 Baseline Compressor Model Development

### 4.1 Iterative Design Approach

A refined baseline design was required to conduct a subsequent optimisation study. Hence, an iterative inverse design approach was adopted to achieve desired performance characteristics. This included the total pressure rise, efficiency, structural integrity, and mass. Firstly, MATLAB®-based 1D models for the inducer, impeller, and volute were constructed to output parameters and geometries required by the CFTurbo® turbomachinery software. Once a 3D compressor model had been established, CFTurbo® was linked with ANSYS® CFX and the CFTurbo® FEA extension to determine the flow and structural performance. If the results did not comply with design requirements, input parameters were modified to initiate an iteration. By using ANSYS® in conjunction with CFTurbo®, an efficient workflow was established for quick adjustments. A flowchart depicting the iteration loop is shown in Figure 9.

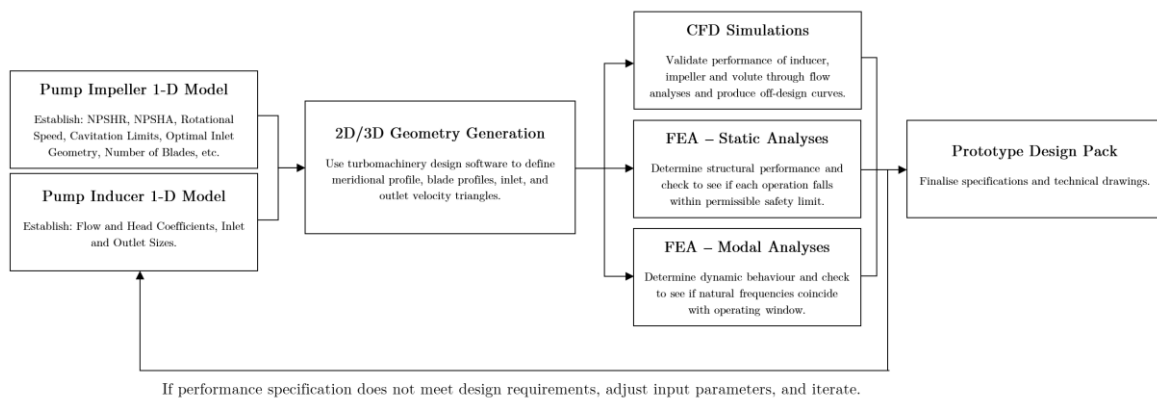


**Figure 9:** Iterative inverse design process for the HTP compressor. Adapted from [F].

### 4.2 1D Model Design Tool

The code structure consists of a top-level function which feeds user-specified inputs, relating to the compressor design point and overall geometry, into separate component scripts. These then output the flow coefficients, performance parameters, and blade angles required by CFTurbo®, using the steady-state and empirical equations presented in §2.5. The top-level inputs are the shaft speed, mass flow rate, fluid density, total pressure rise, and the inducer-impeller energy fraction. Figure 10 illustrates the velocity triangles used in the construction of the 1D model.

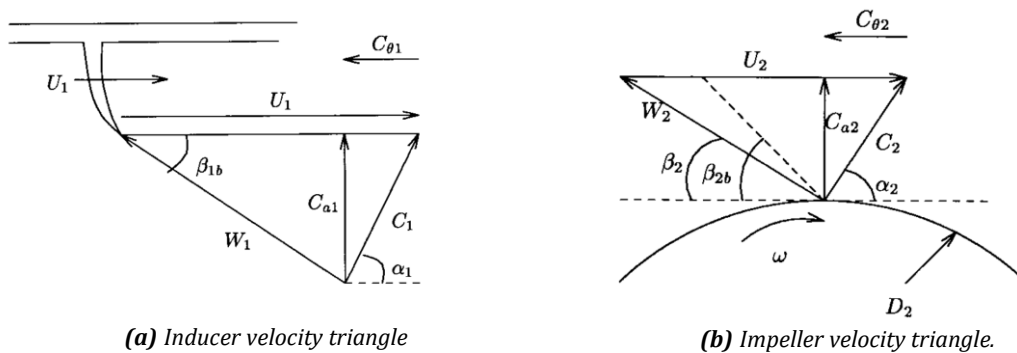


**Figure 10:** Velocity triangles used as the basis for the 1D preliminary compressor model [G].

The respective inputs and outputs for each 1D component model are summarised in Table 2. All 1D model code is provided in Appendix A.

**Table 2:** 1D model code structure – script inputs and outputs.

1D Model	Inputs	Outputs
<b>Inducer</b>	Shroud Diameter at inlet/outlet Hub-shroud Ratio at inlet/outlet Preliminary efficiency Blade Count	Flow Coefficient Work Coefficient $NPSH_R$ $NPSH_A$ Inlet Blade Angles, $\beta_{b1}$ Outlet Blade Angles, $\beta_{b2}$ Specific Speed Specific Diameter
<b>Impeller</b>	Impeller Diameter Hub Diameter Outlet Width Preliminary efficiency Blade Count	Flow Coefficient Work Coefficient Diameter Ratio Outlet Width Ratio Inlet Blade Angles, $\beta_{b3}$ Outlet Blade Angle, $\beta_{b4}$ Specific Speed Specific Diameter
<b>Volute</b>	Outlet Radius Impeller Outlet Velocity Impeller Outlet Radius	Outlet Pipe Diameter  Area Variation Plot  Spiral Contour Plot

Several simplifying assumptions were applied in the creation of this model. These are summarised as follows:

1. Incompressible, steady flow.
2. Inviscid flow.
3. Adiabatic system.
4. Zero pre-swirl at inducer inlet.
5. Axial, uniform inflow.
6. Isentropic expansion.
7. Finite blade span count.
8. Assumed preliminary efficiencies.

The presented preliminary modelling tool provides an efficient approach to generating all specifications which are required to produce a sufficient initial compressor design. The code offers a great amount of flexibility for the initial development stage, and inputs can be easily modified to suit a range of performance requirements, operating conditions, and fluids.

### 4.3 CFTurbo® Model Development

#### 4.3.1 Generated 2D Meridional Geometry

For each iteration, the outputs from the 1D model were then inputted into CFTurbo® to generate useable compressor geometry. A 2D meridional model was then constructed which included all elements required for ANSYS® CFX. This included the inducer, impeller, volute, and inlet and exit pipes to ensure steady conditions at either boundary. Figure 11 depicts the meridional view of the baseline compressor.

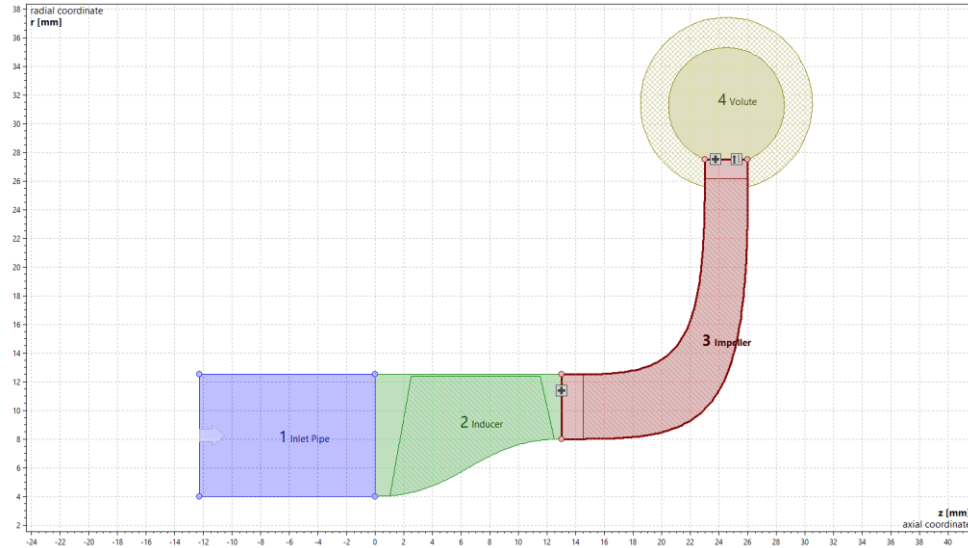
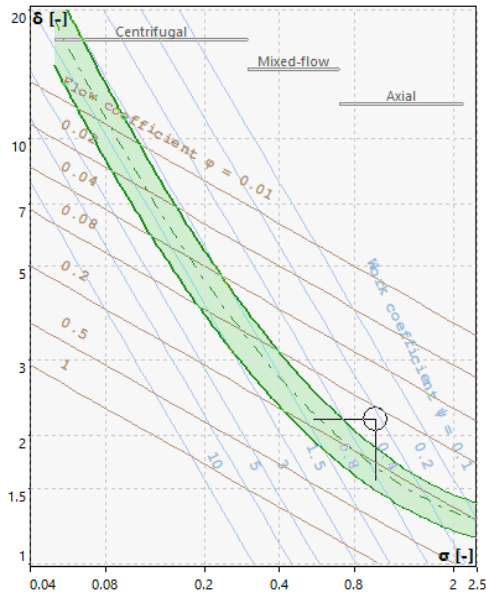


**Figure 11:** Compressor subassembly meridional view. Dimensions are included for reference.

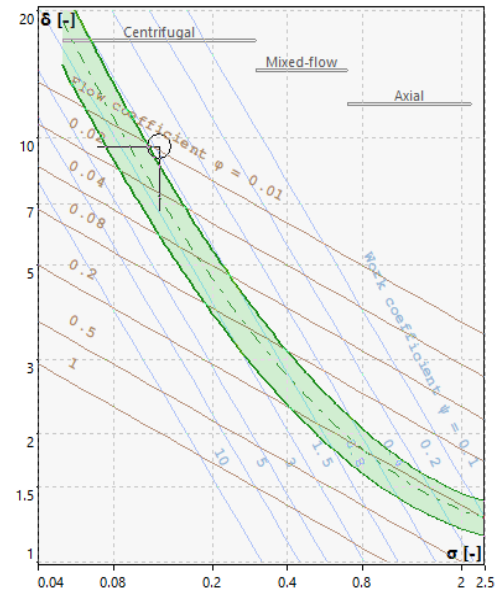
An unshrouded inducer design was selected to limit the outboard mass of the component and reduce blade root stress concentrations. To compensate for the loss in performance experienced by choosing an unshrouded design, a low tip clearance of  $0.1\text{mm}$  was specified to ensure tip leakage flows were kept to a minimum. For the purposes of the experimental prototype, zero inflow swirl was also specified. When concerning the meridional contour as shown in Figure 11, straight line LE and TE profiles were used, and a Bézier curve with tangential start and end conditions was defined for the hub geometry. The drive shaft was modelled at the inner surface of the inlet pipe.

For the impeller, a shrouded design was opted for, with upstream swirl enabled to account for the inducer outflow. Similarly, straight line LE and TE were chosen. No secondary flow paths were created for either the inducer or impeller. Finally, to construct the volute geometry, a simple circular cross-section, with a linear area progression, was used for both the spiral contour and the exit diffuser. This rudimentary approach helped to avoid additional complexity at the baseline design stage, where too many variables could have limited progress and configuration control.

At this stage, Cordier plots were also generated to monitor how the closely the inducer and impeller designs coincide with the optimum condition, as defined by extensive experimental data and empirical analysis of proved turbomachinery designs [34]. Relative coordinate axes were used, which displayed specific diameter  $\delta$  against specific speed  $\sigma$ . Straight lines for the work coefficient  $\psi$  and the flow coefficient  $\varphi$  are also displayed. The Cordier plots for the baseline inducer and impeller designs are given in Figure 12.



(a) Inducer Cordier plot.

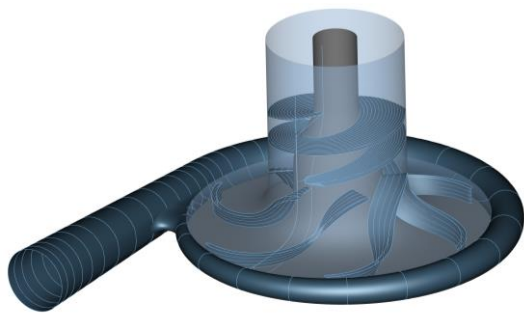


(b) Impeller Cordier plot.

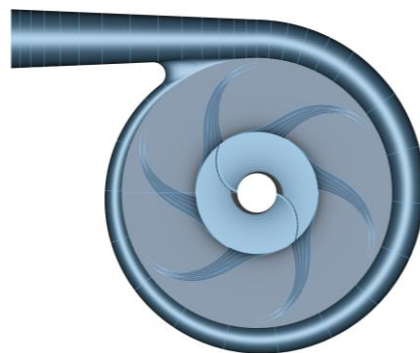
**Figure 12:** Respective Cordier plots for the inducer and impeller.

#### 4.3.2 Generated 3D Geometry

Once the compressor meridional geometry had been finalised for each iteration, a 3D compressor model was generated. Additional steps were required to establish final blade geometry. For both the inducer and impeller, a default mean line blade setup was specified for the meridional coordinate positioning with respect to the tangential coordinate, as a full blade mean line optimisation was out of the scope of this project. Secondly, as recommended by the NASA Design Criteria, trapezoid blade thickness distributions were modelled [21]. Finally, inducer blade edge types included an elliptical LE and a straight TE, while impeller blade edge types were both specified as elliptical. Figure 13 shows the baseline compressor 3D model. Hub and shroud solids were not enabled to ensure smooth compatibility with ANSYS® CFX, whereas these were created for use in the CFTurbo® FEA software.



(a) Compressor ISO view.



(b) Compressor Top-view

**Figure 13:** View of generated 3D compressor geometry from CFTurbo®.



## 4.4 Internal Flow Analysis Setup

Flow simulations were conducted using ANSYS® CFX 2022 R1 under a student licence.

### 4.4.1 Geometry Construction

The fluid domain of each baseline component was exported from CFTurbo® into ANSYS® DesignModeler. All constituent components are shown in Figure 14.

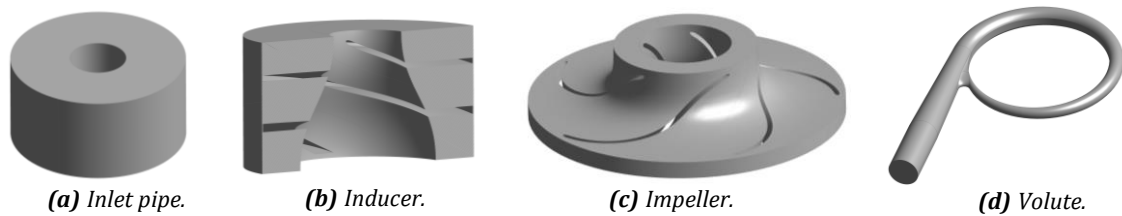


**Figure 14:** Component flow domains. A section view of the inducer has been used for reference.

Named Selections were assigned at this stage for component inlet and outlet boundaries, domain and interface definitions, blade surfaces, hub and shroud surfaces, and volute walls. This provided an efficient setup within ANSYS® CFX-Pre.

### 4.4.2 Simulated Fluid

All analyses utilised the 90% concentration HTP properties summarised in Table 1. The fluid was modelled as a constant property liquid, as opposed to specifying an aqueous solution through mass fractions. For the purposes of this project where only overall pump performance is concerned, this assumption was acceptable.

### 4.4.3 Solver Settings

For all analyses, steady state, incompressible flow was assumed. To capture the rotational motion of the drive shaft, inducer, and impeller, the Multiple Reference Frame (MRF) method was adopted. The inlet pipe, inducer and impeller flow domains were modelled under a rotating reference frame at the desired angular velocity. The drive shaft, inducer hub, impeller hub and shroud, and all blade surfaces were defined as smooth, non-slip walls with zero velocity. The inlet pipe outer surface and inducer shroud were defined as counter rotating walls. The volute and exit pipe domains were modelled under a stationary reference frame.

The impeller-outlet and volute-inlet interface was setup using General Connection interface model, which incorporated a constant total pressure Mixing-Plane. Instead of assuming a fixed relative position of the impeller blades, the Mixing-Plane model performs a circumferential averaging of the fluxes through bands on the interface. Steady state solutions are then obtained in each reference frame [37]. The Frozen Rotor approach, however, provides a direct coupling, imposing the local flow conditions from one row to the other, and vice versa. Supposedly providing a more accurate representation of exit flow behaviour, the absence of inertia does lead to physical inconsistencies in the form of artificial wakes, so was omitted for this study [37,38].

The Shear Stress Transport (SST) turbulence model was used because it has been reported to predict flow separation more accurately than the k-epsilon model, as well as exhibiting good behaviour in adverse pressure gradients [3]. Temperature variation across the compressor was not modelled; flow was assumed isothermal at 25°C. As the temperature field is decoupled from the velocity and pressure fields in incompressible flow, isothermal flow is a reasonable assumption.

#### 4.4.4 Boundary Conditions

For the nominal design point, a uniform total pressure of 4.15 *bar* and a mass flow rate of 8.00 *kg/s* was prescribed at the inlet and outlet boundary, respectively. This ensured the flow characteristics matched the compressor design requirements. Both were defined in the stationary reference frame with medium turbulence intensity (5%), and the respective planes were positioned far enough from the inducer and volute spiral to ensure a fully-developed velocity profile [3]. Both boundary conditions are shown in Figure 15.

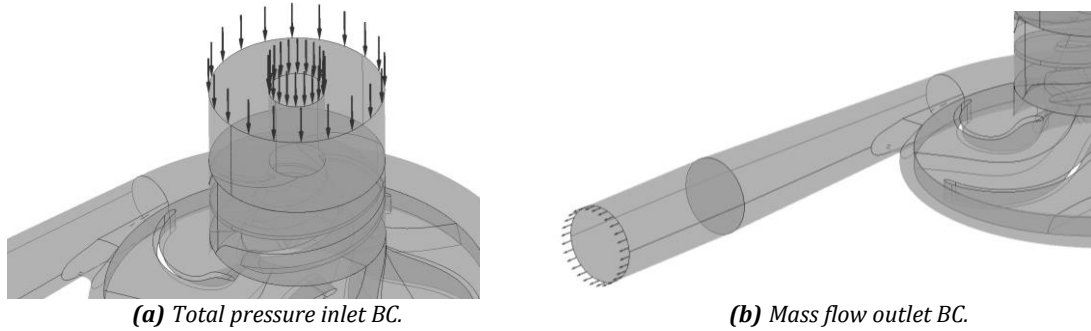


**Figure 15:** Prescribed boundary conditions (BCs) for the compressor model.

#### 4.4.5 Mesh Construction and Independence Study

A mesh independence study was conducted to determine result sensitivity with respect to mesh density, and to construct an optimum mesh which provides a balance between accuracy and computational performance. Four meshes were generated, each with increasing levels of quality. This was achieved by decreasing the element size, and the curvature and proximity minimum sizes. Modification of the curvature function reduced violation of complex geometries, whilst the proximity function helped regulate volumetric gaps between elements [37]. Due to the constraints of the student licence, there was an imposed mesh refinement limit on each component.

An inflation layer was also applied to all blade, hub, shroud, and volute surfaces. This aided in a more accurate boundary layer resolution by inflating the mesh to a specified number of layers from the wall surfaces [37]. Maximum inflation layer thicknesses were set at 0.5*mm* for the inlet pipe, impeller, and volute surfaces, but a thickness of 0.1*mm* was specified for the inducer shroud to account for the tip clearance gap. The inflation layer count was increased in the mesh study to improve boundary layer representation. This was varied from 4 to 10 for the rotational domain, and from 4 to 7 for the stationary domain.

Table 3 summarises the characteristics of each generated mesh. Preliminary simulations were run to obtain elapsed solver convergence times. This provided an additional metric to compare each mesh setting.

**Table 3:** Mesh characteristics for each quality setting.

Parameter	Setting 1	Setting 2	Setting 3	Setting 4
Global Node Count	256,765	346,289	374,488	436,656
Global Element Count	732,620	1,034,309	1,106,863	1,248,336
Average Global Skewness	0.286	0.279	0.271	0.247
Average Global Orthogonality	0.694	0.707	0.718	0.744
Solver Convergence Time	00:07:30	00:10:12	00:11:28	00:13:56

The two primary metrics used to assess mesh quality were global average skewness and orthogonality. Higher mesh quality concerned global average skewness values which were below 0.95 and global average orthogonality values which were greater than 0.1 [39]. Setting 4 produces the highest quality mesh in terms of these two parameters.

Furthermore, all meshes were assessed based on the average  $Y^+$  values through. The average  $Y^+$  values across the entire flow domain for each mesh setting are summarised in Table 4. The SST- $k\omega$  turbulence method provides increased accuracy outside the range of  $5 < Y^+ < 20$ . For  $Y^+ > 20$ , a wall function is employed for improved representation of the velocity profile, whereas for  $Y^+ < 5$ , the viscous boundary sublayer is resolved [37]. All meshes demonstrated reasonable  $Y^+$  values.

**Table 4:** Global average  $Y^+$  values.

Mesh Setting	Average $Y^+$ Value
1	57.9
2	54.5
3	48.6
4	34.2

Using the preliminary simulation results for the total pressure rise across the compressor, a mesh convergence plot was produced, as shown in Figure 16. Overall, the results are shown to be mostly mesh independent, with convergence being displayed after approximately one million elements.

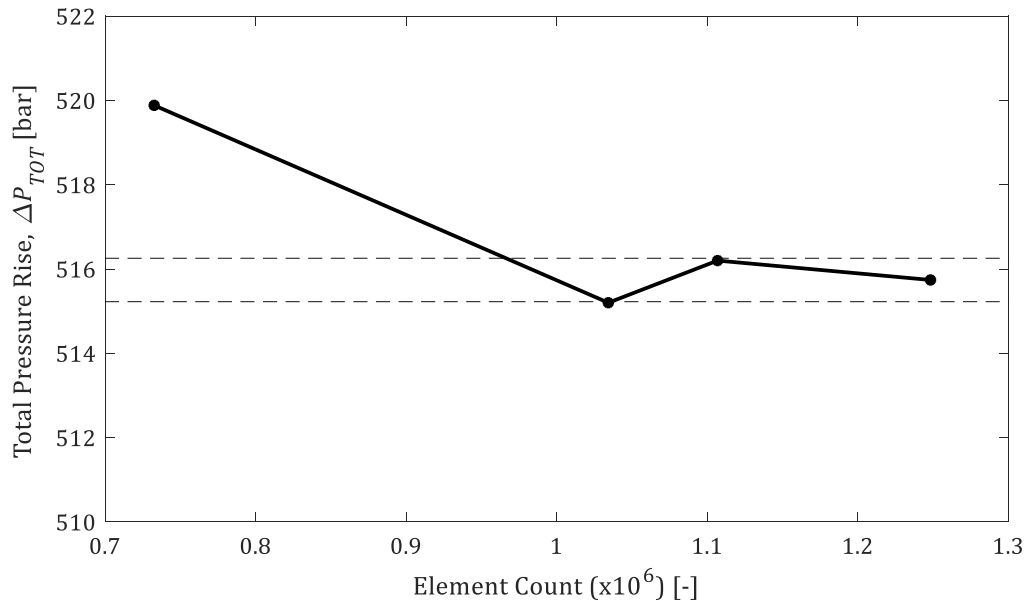
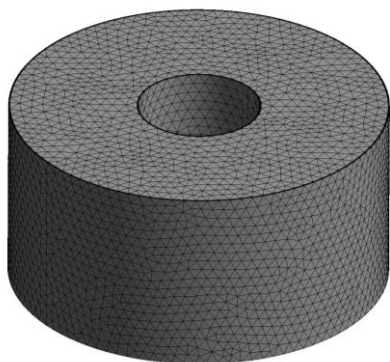
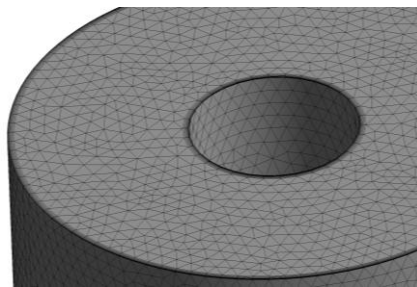


**Figure 16:** Mesh convergence study concerning the total pressure rise against element count. A 0.1% error band has been included for reference.

Given the higher mesh quality in terms of skewness and orthogonality, and sufficient  $Y^+$  value, Setting 4 was utilised for further simulation, despite the minor increase in solver time. The final meshes for each component, and respective inflation layers, are depicted in Figure 17.



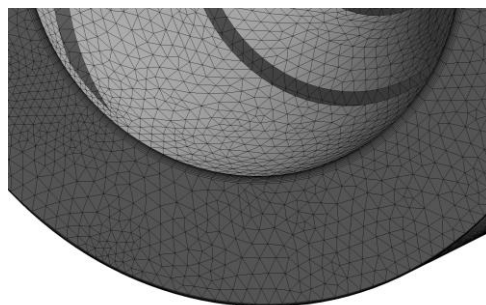
**(a)** Inlet pipe mesh.



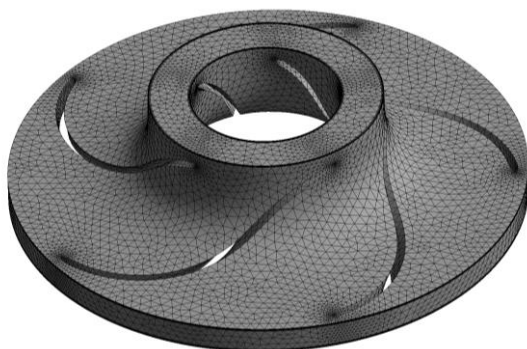
**(b)** Inlet pipe inflation layer.



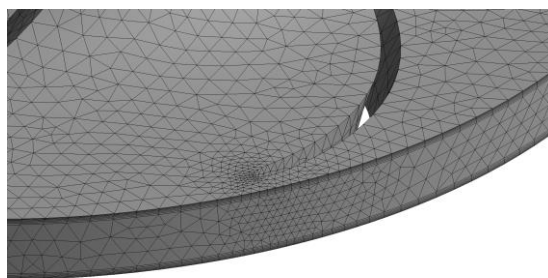
**(c)** Inducer mesh.



**(d)** Inducer inflation layers.



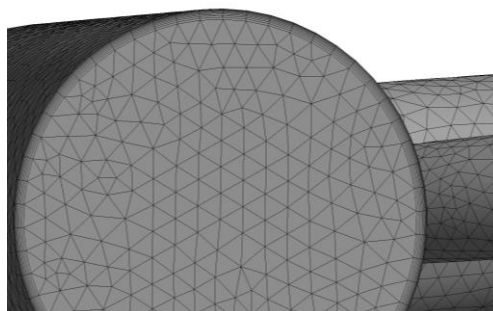
**(e)** Impeller mesh.



**(f)** Impeller inflation layers.



**(g)** Volute mesh.



**(h)** Volute inflation layer.

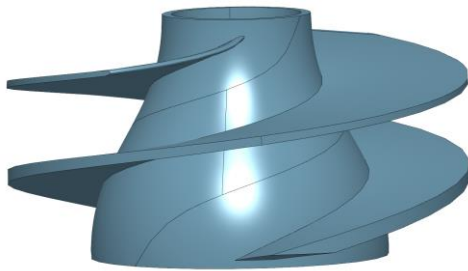
**Figure 17:** Generated component meshes using Setting 4.

## 4.5 Structural Analysis Setup

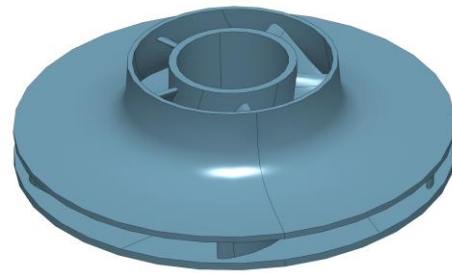
To determine the structural performance of the baseline inducer and impeller designs, static load analyses were conducted for the nominal operational case using the CFTurbo FEA® module. The purpose was to also highlight aspects of the initial geometry which could be optimised for improved structural integrity and mass.

### 4.5.1 Geometry Construction

The baseline geometry is shown in Figure 18. Material domain models were outputted directly from CFTurbo® after modelling hub and shroud solids. Rotational axes were preserved to construct the global coordinate systems.



(a) Inducer geometry.



(b) Impeller geometry.

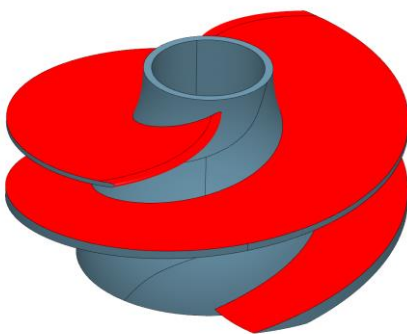
**Figure 18:** Overview of the baseline geometry used for the initial static analyses.

### 4.5.2 Simulated Loads and Supports

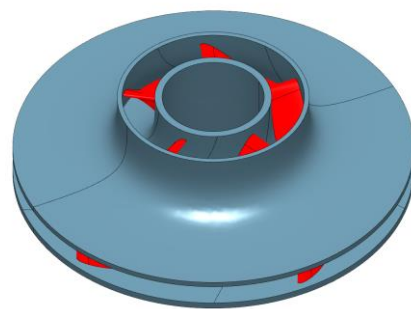
According to the NASA Design Criteria, the two critical loads which both components endure are the centrifugal and blade pressure loads [21]. Therefore, the nominal operating speed of 90,000 *rpm* was assigned. Area-averaged pressure loads were then obtained for the suction and pressure surfaces from ANSYS® CFX-Post. The magnitudes of which are tabulated in Table 5. The inducer and impeller load cases are illustrated in Figure 19. Averaged pressure values will be an over-estimate of the actual distribution, but due to the conservative approach, this was considered acceptable.

**Table 5:** Summary of PS and SS pressure values to construct the blade loading condition.

Component	Inducer		Impeller	
Surface	Pressure Side	Suction Side	Pressure Side	Suction Side
Average Pressure [MPa]	1.27	0.886	17.7	9.15



(a) Inducer load case – centrifugal and pressure.



(b) Impeller load case – centrifugal and pressure.

**Figure 19:** Established load cases for the baseline static analyses.

Fixed supports were assigned to the hub section of each component to simulate the constrained hub-shaft interface. These are highlighted in Figure 20.

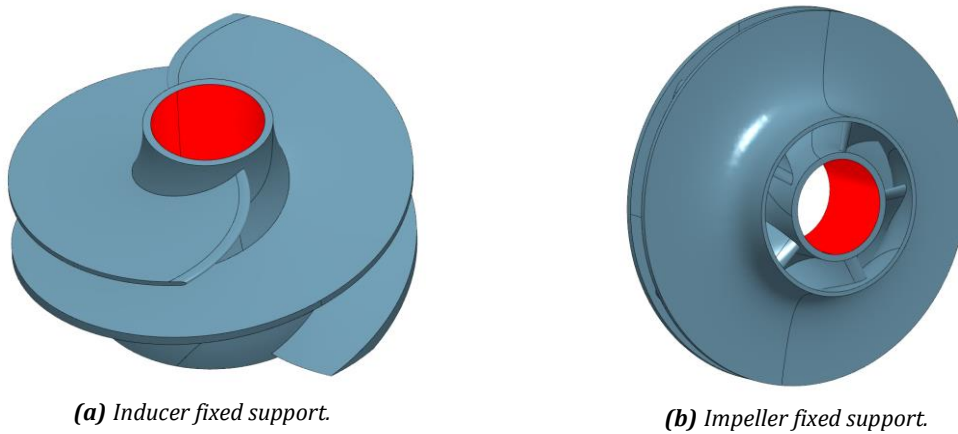


**Figure 20:** Component BCs on respective hubs.

#### 4.5.3 Material Selection

For the baseline model, it was decided that Inconel 718 would be a suitable choice for the inducer and impeller baseline prototypes due to its superior tensile, fatigue, and rupture strength properties [3,17]. The material specification is based on a post-hardened state through precipitation-hardening heat treatments [17]. The material properties used as inputs in CFTurbo FEA® are summarised in Table 6.

**Table 6:** Inconel 178 isotropic material specification for CFTurbo FEA®.

Property	Value
Young's Modulus, $E$	208 GPa
Poisson's Ratio, $\nu_{PR}$	0.31
Tensile Yield Strength, $\sigma_y$	1100 MPa
Ultimate Tensile Strength, $\sigma_{UTS}$	1300 MPa
Density, $\rho_{mat.}$	8820 kg/m <sup>3</sup>
Thermal Expansion Coefficient, $\alpha$	$1.28 \times 10^{-5} \text{ K}^{-1}$

A permissible stress of 935 MPa ( $0.85\sigma_y$ ) was imposed for both components. This was set higher than half the yield strength because of the conservative modelling of the blade pressure distribution. Material behaviour was modelled as linear elastic, with isotropic properties assumed throughout. This is considered a limitation of this study and has highlighted an opportunity to further the analysis.

#### 4.5.4 Element Sensitivity Study

To assess the element sensitivity of both the inducer and impeller models, a study was conducted to monitor how the results vary between linear and quadratic element types. A very fine mesh pre-set was first applied and then the element type varied. Key results were collected to present a comparison. Tables 7 and 8 summarise the values for the inducer and impeller, respectively.

**Table 7:** Inducer element sensitivity study results.

Element Type	Max. Stress	Min. Stress	Max. Displ.	Max Strain
First Order (Linear)	408MPa	0.431MPa	0.266mm	$1.09 \times 10^{-3}$
Second Order (Quadratic)	2537MPa	0.128MPa	1.01mm	$9.43 \times 10^{-3}$

**Table 8:** Impeller element sensitivity study results.

Element Type	Max. Stress	Min. Stress	Max. Displ.	Max Strain
First Order (Linear)	1003MPa	2.11MPa	0.05mm	$4.37 \times 10^{-3}$
Second Order (Quadratic)	3043MPa	0.567MPa	0.11mm	$10.5 \times 10^{-3}$

Evidently, both results demonstrate that the use of the quadratic shape function within each element yields a much higher representation of stresses and strains. This is because linear interpolation between nodes does not capture bending behaviour and will, therefore, underrepresent the exhibited stresses. Thus, lower order tetrahedral elements will make the models overly stiff [40]. At the expense of higher computational cost, it was decided to employ the use of quadratic elements in both models to ensure accuracy.

#### 4.5.5 Mesh Independence Study

To check result convergence with increasing mesh fidelity, a mesh independence study was conducted using the quadratic elements. Mesh settings such as minimum element size, element count per curvature radius, and element count per edge were varied to produce a range of meshes. The maximum stress was then monitored. Figure 21 depicts the maximum stress behaviour as the node count is increased. Both plots demonstrated an adequate level of convergence, and the results were found to be largely mesh dependent until node counts of approximately 500,000 were reached. The study indicated node counts of 500,000 and 800,000 are sufficient to capture the structural performance of the inducer and impeller, respectively.

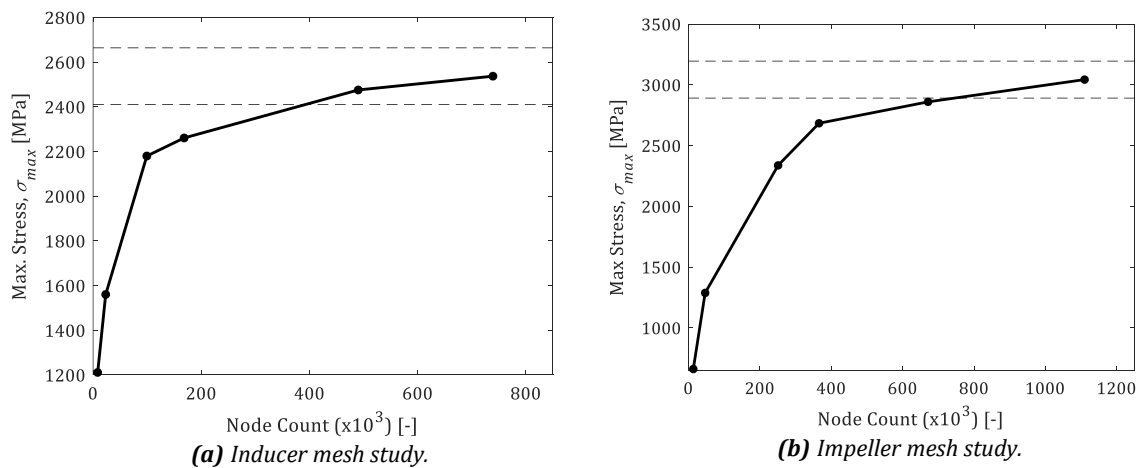


**Figure 21:** Mesh convergence studies showing stress variation with node count. A 5.0% error band has been included for reference.



#### 4.5.6 Generated Meshes

The final meshes for each component are depicted in Figure 22. Refined mesh topology on the respective leading edges is highlighted.

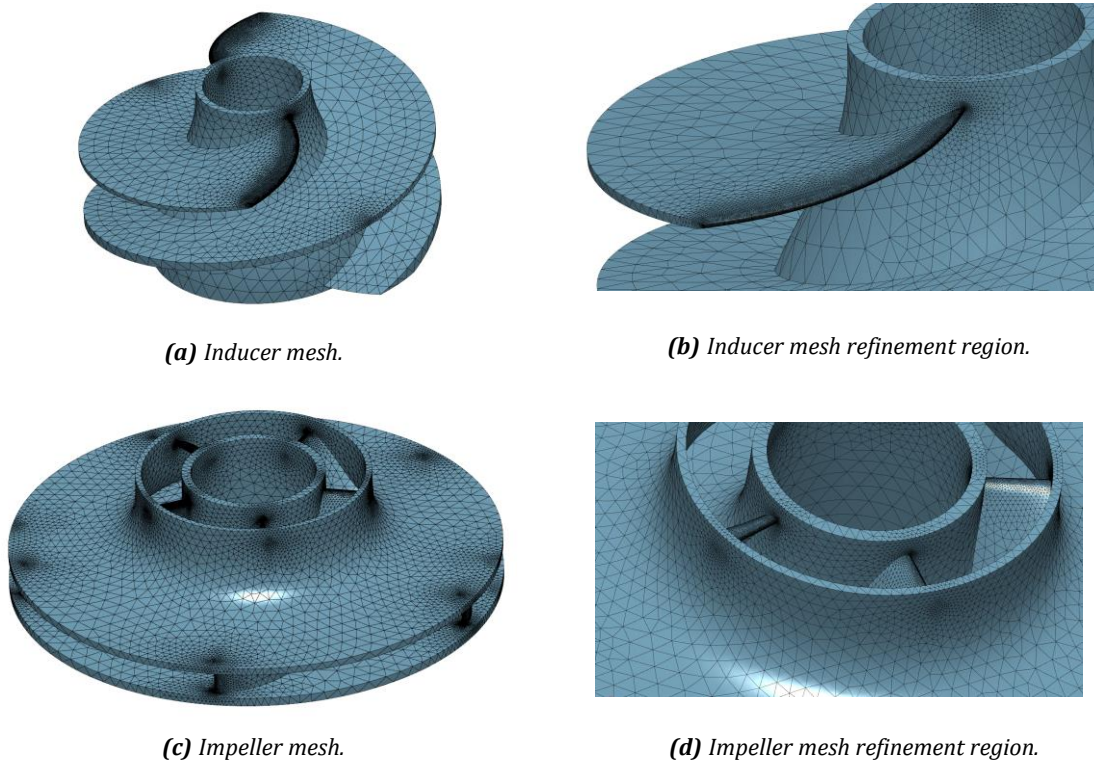


**Figure 22:** Generated component meshes and topology refinement regions at respective LEs.

The final node and element count for both meshes are given in Table 9.

**Table 9:** Inducer and impeller mesh summaries.

Component	Node Count	Element Count
Inducer	498,044	340,993
Impeller	806,875	551,536

To provide a final verification of the mesh quality, the aspect ratio distribution across all elements was obtained. These are shown in Figure 23.

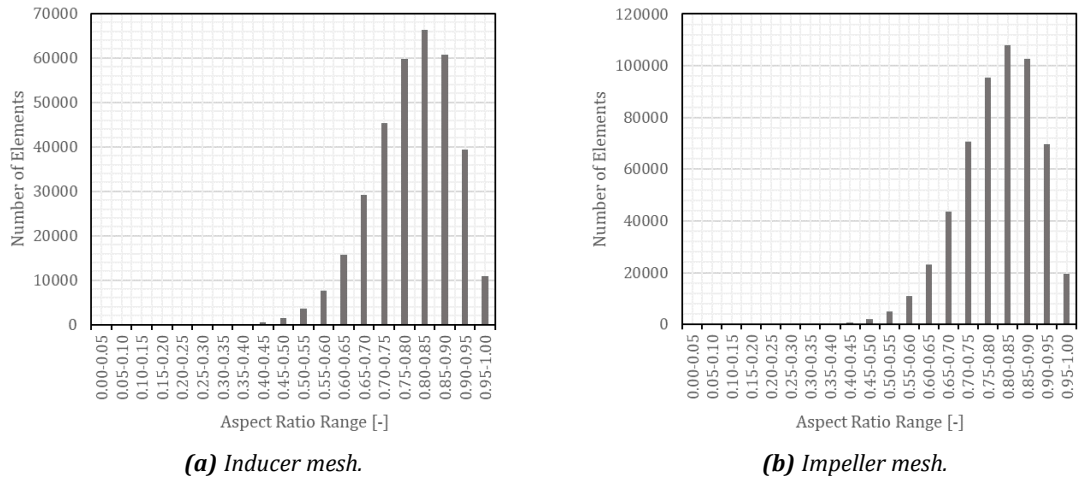


**Figure 23:** Aspect Ratio distribution for both generated meshes.



Both meshes displayed good quality in terms of element aspect ratio, with all elements meeting the imposed limit of 0.30. Aspect ratios above 0.70 were considered desirable, as per K-J.Bathe's suggestion in Finite Element Procedures [40]. The inducer and impeller mesh achieved 84.5% and 82.9% of elements above this target, respectively. This was deemed acceptable.

#### *4.5.7 Modal Analysis Setup*

A modal analysis was conducted to determine the inducer and impeller natural frequencies. By comparison with the operating range, it could be determined if excessive vibration would be experienced by either component. This could impinge on fatigue performance and system safety, as well as inducing flow instabilities.

The same mesh settings from the linear analyses were carried forward, as well as the central fixed supports to simulate the hub-shaft interface [41]. Only the first four modes were calculated for each model. Coriolis acceleration was enabled to account for its induced spread in the natural frequency spectrum, ultimately improving the accuracy of the results [42].

# 5.0 Simulated Flow Performance

## 5.1 Design Iterations

Using the approach outlined in §4.1, the compressor underwent three design iterations. The core drivers were obtaining the total pressure rise requirement of 360 bar, and maximising pump efficiency. Table 10 summarises the recorded performance at each iteration. Across all revisions, major design changes included a reduction in the impeller outlet diameter from 65mm to 55mm, a decrease in blade count from six to five, blade angle adjustments, and refinement of tongue and volute exit geometry. Figure 24 shows the total pressure contour and velocity streamline plots at the pump mid-plane for the nominal operating speed.

**Table 10:** Result summary for each design iteration.

Design Iteration	Total Pressure Rise [bar]	Efficiency [-]
1	706.6	0.685
2	627.8	0.770
3	511.6	0.811

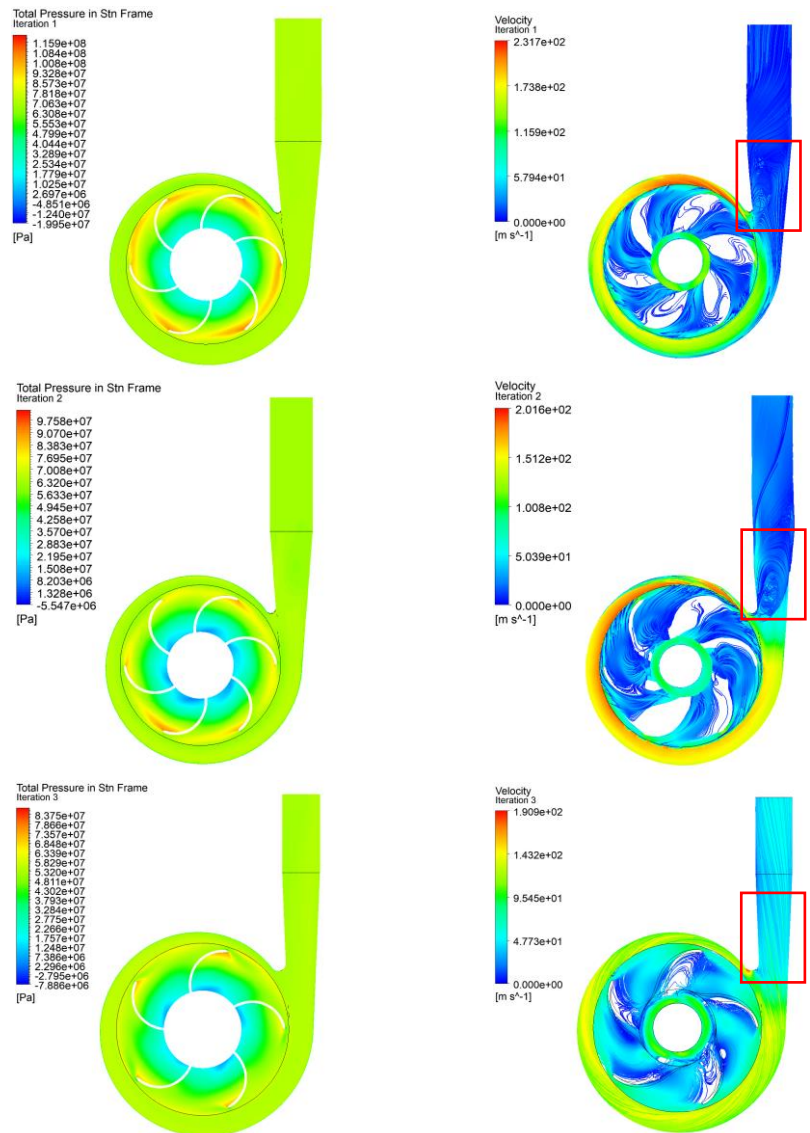


**Figure 24:** Total pressure contour plots and velocity streamlines at the impeller mid-section. Iteration numbers are provided in the contour legend.

The initial results demonstrated the compressor was overperforming significantly in terms of the total pressure rise, with Iteration 1 producing almost double the required value. Although, comparison of the pressure contour plots in Figure 24 verifies the significant reduction in volute outlet pressure achieved by the iterative design approach. This reduction was mostly attributed to impeller diameter adjustments and introducing less aggressive impeller outlet blade angles. However, the Iteration 2 pressure contour shows large regions of low-pressure about the central hub, which has high potential to incite cavitation. Blade cavitation is typically created in the proximity of the LE on the blade suction side, and acts as an extra-blockage, in addition to that caused by the blade solidity. The main detrimental effect of blade cavitation is the increased hydrodynamic losses caused at the impeller inlet, which diminish the delivered pressure rise [1]. Despite these being decreased in Iteration 3, there was an obvious decline in this aspect of the performance characteristics overall. To truly appreciate this behaviour, further study is required with the use of a cavitation model to quantify its effects [3].

Based on the velocity streamline plots in Figure 24, lower velocities are apparent in the volute channel in Iteration 3, compared to earlier revisions. This is because of the lower tangential velocity imposed on the fluid as a result of the decreased impeller diameter. Furthermore, a more gradual increase in circumferential velocity is apparent. Iteration 3 also gives higher velocities in the impeller blade channels; however, low velocity regions are still present, which promotes unsteady flow [1]. This is visible from the vortices on both the pressure and suction blade sides. Highlighted in Figure 24 is the flow behaviour in the volute diffuser for each iteration. Far less turbulence is evident in Iteration 3, compared to the first two configurations. This is explained by the increase of volute tongue fillet size causing less disturbance to the volute channel flow.

Due to restricted timescales, further iterations were not possible, and the design was unable to converge on a configuration which complied with all design requirements. Therefore, the third iteration was carried forward to be used as the baseline compressor model. This will be utilised for further performance assessments and an optimisation study. Nevertheless, iterative performance improvements have been successfully demonstrated, which validates the outlined methodology framework.

## 5.2 Baseline Compressor Performance

This section aims to quantify overall performance of the baseline compressor for three operating conditions outlined by PU: low, nominal and redline power modes. The characteristics of the baseline compressor are summarised in Table 11 for all three cases.

**Table 11:** Characteristic pump performance for nominal and off-design conditions.

Parameter	Unit	Low Power	Nominal Power	Redline Power
Shaft Speed	rpm	75,000	90,000	100,000
Pump Mass Flow Rate	kg/s	6.5	8.00	8.90
Power Requirement	kW	213	363	497
Torque	Nm	27.1	38.5	47.5
Pump Efficiency	-	0.798	0.811	0.781
Pump Total Pressure Rise	bar	366.1	515.7	610.9
Inducer Total Pressure Rise (Percentage of Pump $\Delta P_{TOT}$ )	bar	31.0 (8.5%)	26.2 (5.1%)	20.5 (3.4%)
Pump Inlet Total Pressure	bar	4.15	4.15	4.15

Calculated volute outlet pressures from the off-design power modes vary significantly. An increase in total pressure rise of 18.5% is obtained from running at redline power, with a decrease of 29.0% for the low power mode. Evidently, the PU pressure requirement could be achieved by running the compressor at a reduced shaft speed and mass flow rate. This demonstrates the high versatility of the proposed design. The nominal power mode provides an optimum pump efficiency, with a 3.0% loss identified for redline power.

The nominal power requirement of 363 kW correlates strongly with the performance predictions from the 1D model, which gave 350 kW. The difference between which can be explained by the exclusion of further hydraulic and volumetric efficiencies, and viscous effects, which CFTurbo® accounts for. This validates the initial design stages.

In terms of inducer performance, a higher outlet total pressure was obtained through low power operation, with the energy fraction also falling within the desired 6.0-12.0% range. Figure 25 illustrates how this could improve impeller cavitation, with higher pressure regions observed on the blade suction sides. Conversely, nominal and redline operations exhibit lower inlet pressures, which could promote inferior cavitation performance.

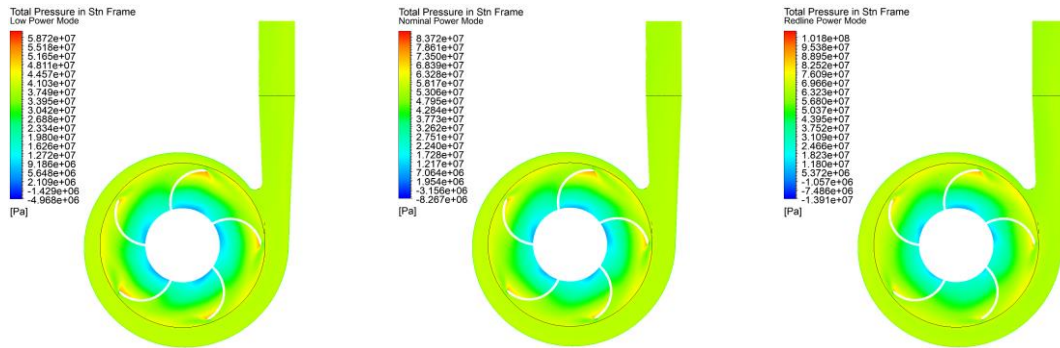


**Figure 25:** Total pressure contour plots at the impeller mid-section. Power modes are provided in the contour legend.

A compressor performance map was produced for all three power modes. This gives the total pressure rise across a range of mass flow rates, both normalised by the design point of 360 bar and 8.00 kg/s. This is shown in Figure 26.

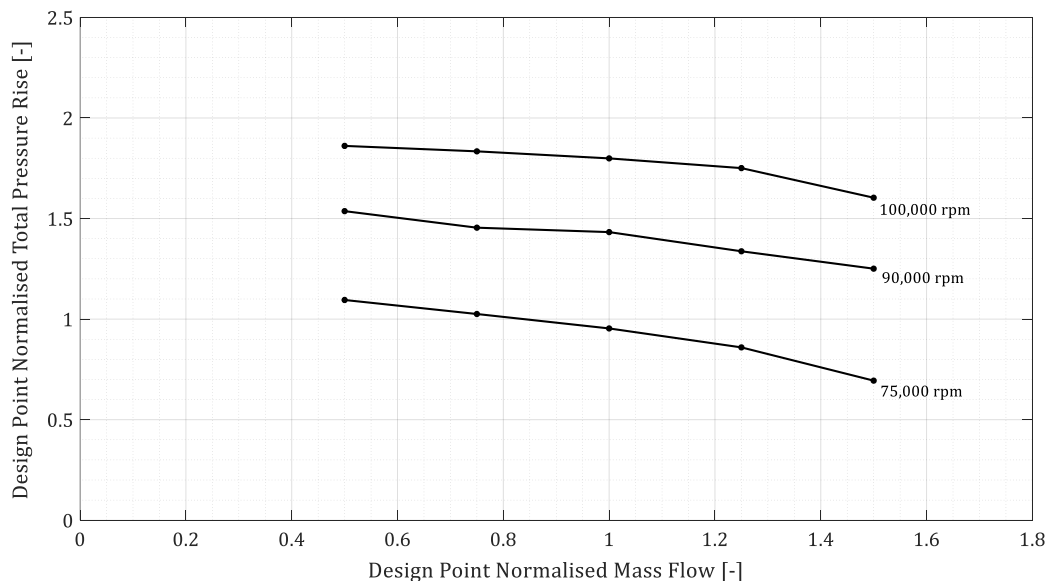


**Figure 26:** Compressor performance map for three speed modes. Results have been normalised by the design points of 360 bar and 8.00 kg/s.

Analysis of the performance map confirms running the compressor at a shaft speed of 75,000 *rpm* and a mass flow rate of 6.00 *kg/s* would comply closely with the PU pressure rise requirement. The corresponding efficiency of this mode was calculated as 77.4%. To capture the full throttle characteristics, further data points should be obtained to include the lines of constant efficiency and lower shaft speeds.

## 6.0 Simulated Structural Performance

### 6.1 Static Load Performance

This section summarises the static load analysis results for the baseline inducer and impeller designs. This acted as a gauge for their initial structural performance, and highlighted aspects of the geometry to be refined in a further optimisation study. Figure 27 shows the obtained von Mises stress distribution for the impeller.

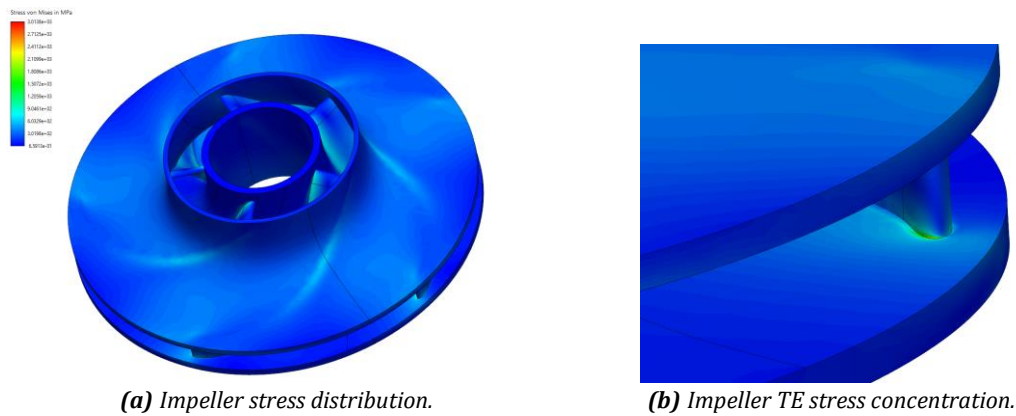


**Figure 27:** Impeller static load results depicting endured stresses.

It is apparent that the stress distribution across the impeller shroud surface is low and evenly spread. However, stress concentrations located along the hub position and trailing edge of the blades are critical. The maximum stress concentration is located on the blade trailing edges, with a value of 3014 *MPa*. This exceeds the Ultimate Tensile Strength (UTS) of Inconel 718, and will, therefore, fail at the nominal design case. Figure 28 shows the deformed shape.

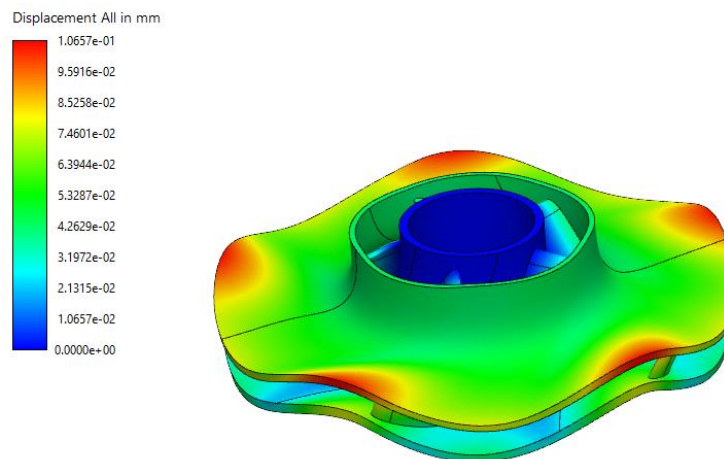


**Figure 28:** Impeller static load results depicting global displacement.  
A deformation factor of 40 has been applied for reference.

A maximum displacement of 0.107*mm* was recorded for the impeller shroud. While the limiting condition is total material failure, the level of deformation was considered acceptable with respect to the component clearances within the compressor assembly.

The von Mises stress distributions for the inducer are given in Figure 29.

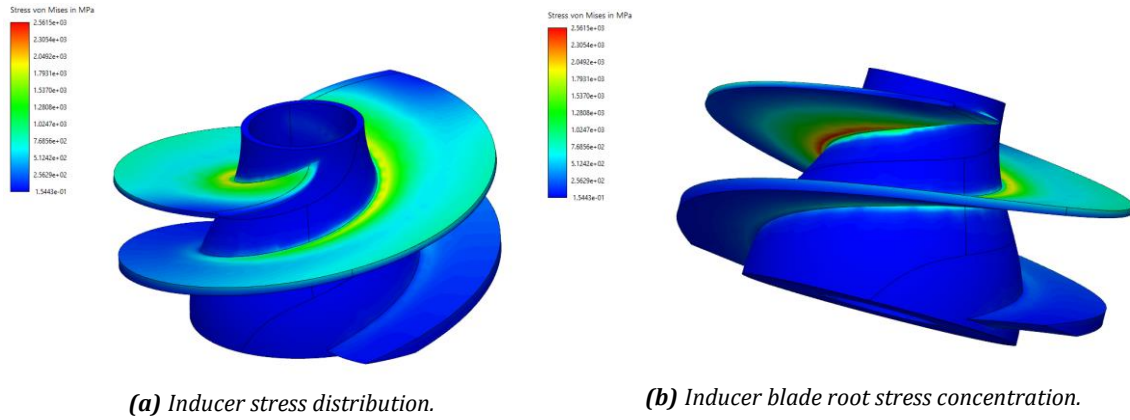


**Figure 29:** Inducer static load results depicting endured stresses.

The inducer exhibited minimal stress across the hub profile, with most distributed across the blade span, particularly towards the leading edge at lower thicknesses. As depicted in Figure 29b, a stress concentration was identified on the pressure side root. This had a maximum value of  $2562 \text{ MPa}$  and was also outside the UTS limits of Inconel 718. Figure 30 shows the inducer deformation.

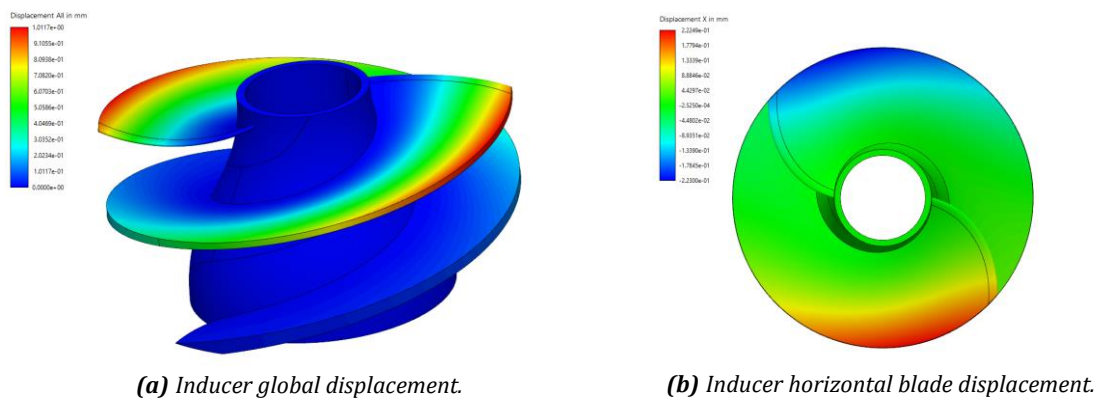


**Figure 30:** Inducer static load results depicting global displacement.  
A deformation factor of 1.0 has been applied for reference.

Across all axes, the maximum displacement was  $1.01 \text{ mm}$ . When considering the horizontal planar deformation, in Figure 30b, a value of  $0.222 \text{ mm}$  was obtained. This exceeds the tip clearance gap of  $0.1 \text{ mm}$  and is, therefore, unsuited for use.

In summary, both components fail structurally outside physical limits, and several improvements were required to ensure operation within the linear regime of the material. These will be explored in the next section as part of an optimisation study. It was proposed that the high stress concentrations were a result of singularities at the impeller TE and inducer blade root. This also explains the low convergence behaviour during the mesh study in §4.5.5. Therefore, fillets will be added to the required geometries during the optimisation study to eliminate the problem [3].



## 6.2 Dynamic Behaviour

The first four inducer and impeller natural frequencies are tabulated in Table 12. Evidently, no resonant frequencies coincide with the compressor operating range of 1250-1670 Hz (75,000-100,000 rpm), and none will be passed through during spool-up.

**Table 12:** Baseline compressor natural frequencies.

Component	Mode Number	Frequency [Hz]
Inducer	1	5,680
	2	5,680
	3	8,105
	4	8,110
Impeller	1	7,865
	2	7,884
	3	8,782
	4	8,801

Closer inspection of Table 12 reveals how the modes are experienced in pairs. This was attributed to the symmetrical geometries of both components. Figure 31 summarises the derived shape for each mode pair.

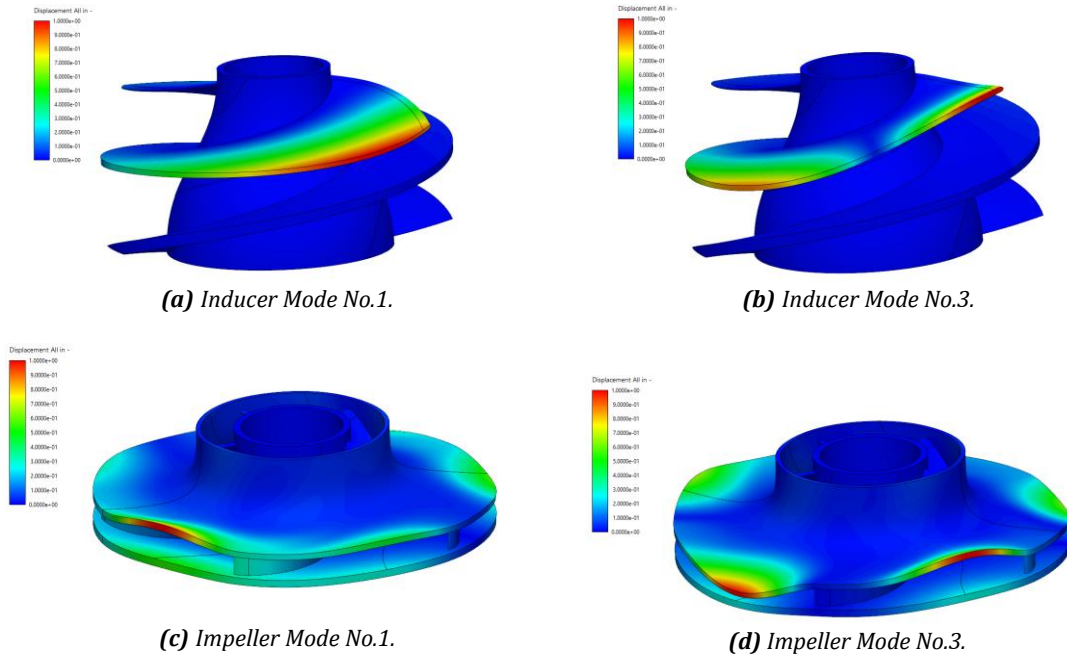


**Figure 31:** Derived natural frequencies for both components, depicting each mode pair.

No concern was raised by this study, as the natural frequencies are much higher than the operating window of the pump, and material failure will occur foremost. However, the results have affirmed the importance of increasing the inducer blade thickness and impeller shroud thickness. This will stiffen the respective structures to increase their load bearing capabilities and natural frequencies.

## 7.0 Optimisation Study

### 7.1 Splitter Blade Integration

Using the baseline compressor model, an optimisation study was conducted. By controlling all design parameters and modifying a single aspect, performance improvements could be truly evaluated. It was proposed that implementation of splitter blades would increase the pump pressure rise and efficiency, for the same input power [43]. Thus, this section covers their integration and the determined performance characteristics.

The inclusion of splitter blades has been reported to reduce blockage at the impeller inlet due to an increased blade channel area. Reduced blockage translates into lower velocities, higher pressures and, hence, reduced cavitation development on the blade suction side, when compared to an impeller with a similar number of full-length blades [1]. Furthermore, splitter blades can promote better flow control within impeller channels by reducing streamline deviation, which leads to more uniform blade loading [1]. As ascertained from the baseline results, the impeller suffers significantly from unsteady flow within the blade channels, as well as low pressure regions at the inlet. This emphasises the value of studying the effects of splitter blades on the compressor performance.

The blade count of the baseline model was increased to six, but incorporated three main blades and three splitter blades. Figure 32 illustrates the change in geometry.

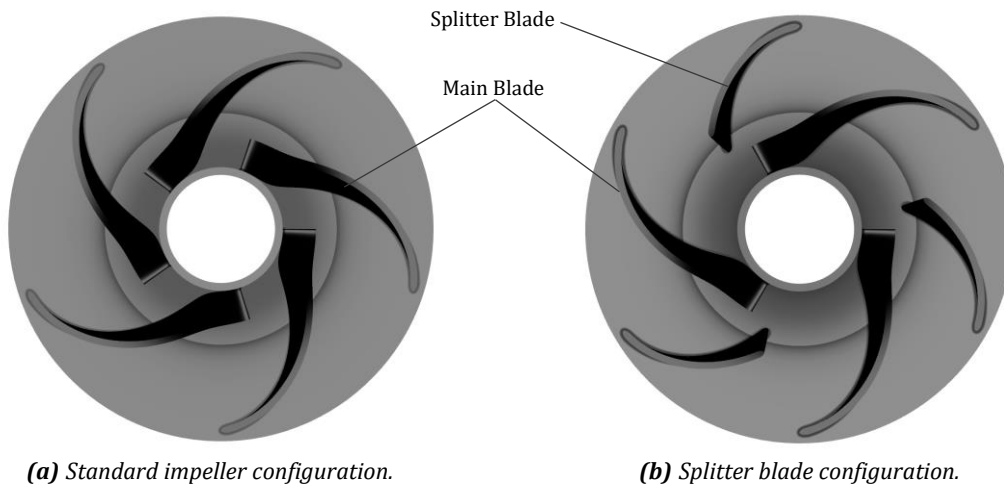


**Figure 32:** Comparison of impeller standard and splitter blade designs.

The splitter blade profile will be equal to that of the main blade to ensure consistency across the study. Even though this has been reported to limit the true potential of splitter blade performance significantly, this has highlighted an opportunity to refine the mean line profile as part of a future study. The meridional position of the splitter blade LE is a critical parameter [1]. Thus, this was selected as the main focus of the optimisation whilst maintaining a fixed TE at the impeller outlet. Figure 33 shows the variation of efficiency with the splitter blade LE meridional position, as a percentage of the total length.



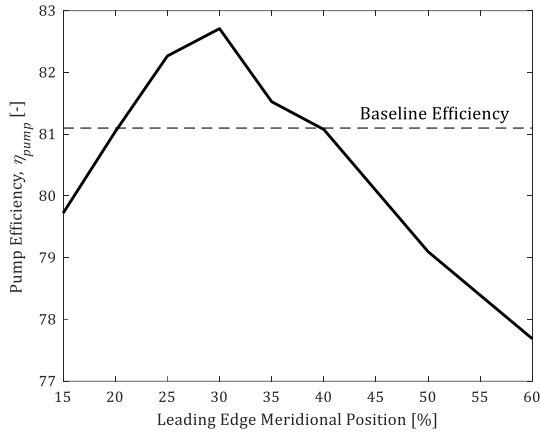


**Figure 33:** Variation of efficiency with LE position.

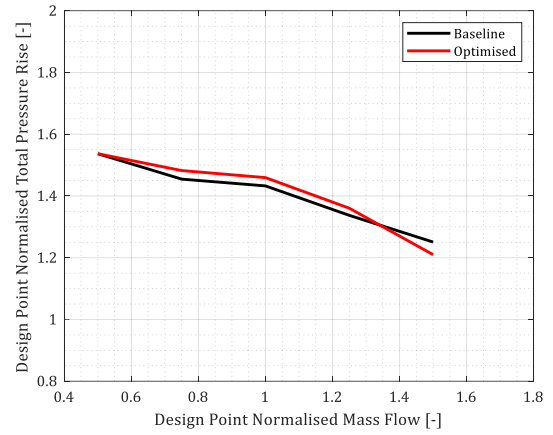


**Figure 34:** Revised compressor performance map.

A clear relationship is apparent between the pump efficiency and LE meridional position of the splitter blades. At lower meridional positions, there is an increase in the blockage at the impeller inlet, resulting in a decreased pressure rise and, hence, lower efficiency. As the splitter blade LE is moved outboard of the impeller hub, the efficiency is increased due to less channel blockage. This reaches a maximum efficiency of 82.7% at 30% meridional position. The efficiency then drops off rapidly at low splitter blade lengths, as the ability to generate a pressure rise is lessened. Overall, an optimal splitter blade configuration was successfully obtained which delivered an efficiency increase of 1.6%.

Figure 34 shows the compressor performance map, with the optimal splitter blade model superimposed. This depicts how the total pressure rise increases to a maximum of 525.4 bar at the nominal 8.00 kg/s mass flow rate, corresponding to a pressure rise improvement of 9.7 bar. Similar margins relative to the baseline case are displayed at lower mass flow rates, but there is a clear decrease in effectiveness after approximately 10.0 kg/s.

To assess the improvement to impeller channel flow quality, streamline plots were produced for both impeller configurations. Figure 35a highlights a zone of separated flow from blade pressure side in the baseline impeller. Streamlines are shown to depart close to the blade LE. Figure 35b demonstrates how the splitter blade encourages streamlines to follow the main blade pressure surface more smoothly. This further validates the benefits of adopting splitter blades within the final proposed compressor design.

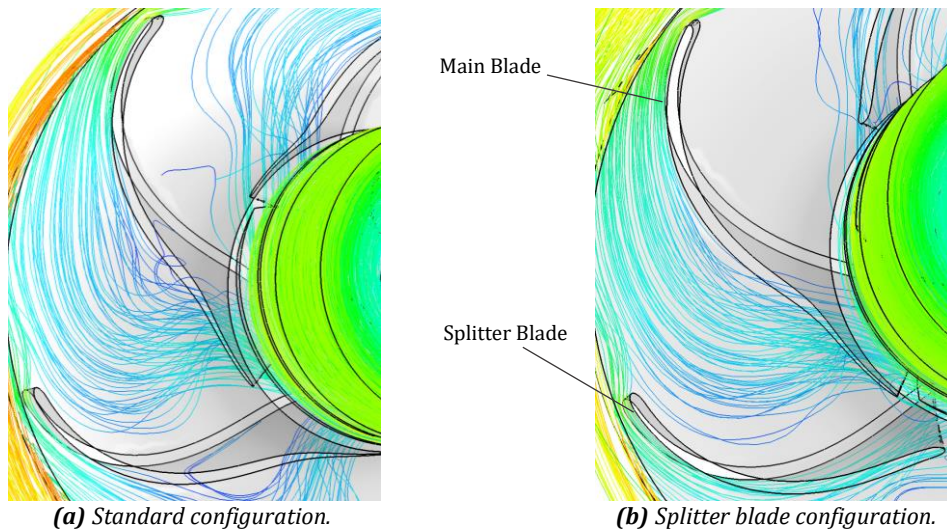


**Figure 35:** Comparison of streamline congruence in standard and splitter blade impeller configurations.

## 7.2 Structural Improvements

### 7.2.1 Component Modifications

Using the results of the baseline static analyses, several improvements were made to the inducer and impeller models to improve their structural performance. For the inducer, blade LE and TE thicknesses were both increased by a factor of two, whilst employing a less aggressive trapezoid thickness distribution to alleviate blade bending towards the LE. Additionally, fillets were added at the blade roots to reduce stress concentrations, but also simulate the geometry produced from CNC machining. Finally, an M6 thread is included on the hub to provide a shaft assembly feature. These changes are illustrated in Figure 36.

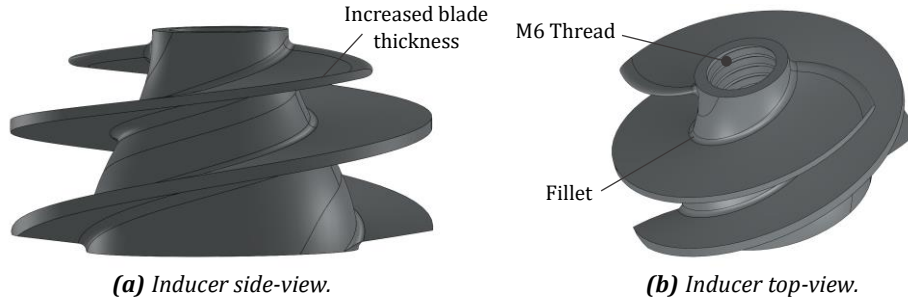


**Figure 36:** Inducer structural modification summary.

To combat the stress concentration on the blade TE, the axis ratio of the TE ellipse was decreased from 3.0 to 2.0. Fillets were also added on the blade edges to reduce stress, and simulate the CNC machining and EB welding result. A mass-reduction feature was also modelled on the hub underside. These modifications are shown in Figure 37.

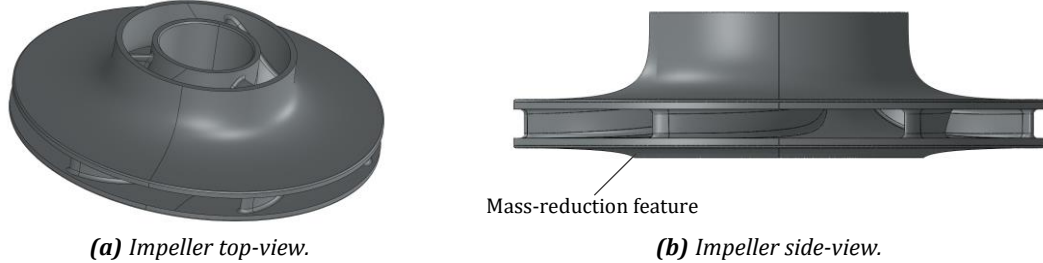


**Figure 37:** Impeller structural modification summary.

It was also decided that the component material should be swapped for stainless steel (17-4 PH Grade) due to its preferable yield strength, Young's Modulus, density, fatigue performance, and machinability. Table 13 outlines all relevant properties for further analyses.

**Table 13:** SS 17-4 PH isotropic material specification for CFTurbo FEA®.

Property	Value
Young's Modulus, $E$	210 GPa
Poisson's Ratio, $\nu_{PR}$	0.30
Tensile Yield Strength, $\sigma_y$	1170 MPa
Ultimate Tensile Strength, $\sigma_{UTS}$	1350 MPa
Density, $\rho_{mat.}$	7750 kg/m <sup>3</sup>
Thermal Expansion Coefficient, $\alpha$	$1.08 \times 10^{-5} \text{ K}^{-1}$

A new permissible stress of 995 MPa ( $0.85\sigma_y$ ) was imposed for both components.

### 7.2.2 Revised Structural Performance

For both components, updated blade pressure distributions were applied. The impeller stress and displacement distributions are shown in Figure 38.

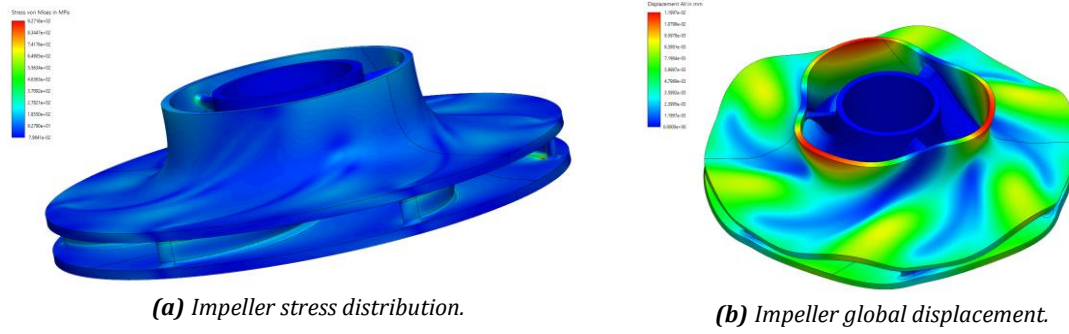


**Figure 38:** Revised impeller structural performance. A deformation factor of 270 is applied to (b).

As a result of the design changes, a reduced maximum stress of  $927\text{MPa}$  was recorded on the blade TE. This falls within the linear regime and permissible stress limit. This was attributed to the use splitter blades, which gave more uniform blade loading. Much lower displacements were also recorded, with a maximum value of  $0.012\text{mm}$  at the shroud inlet. Due to the increased hub and shroud masses, higher stress is present at the blade LE roots, although this is still within operational limits. Figure 39 gives the inducer stress and displacement distributions.

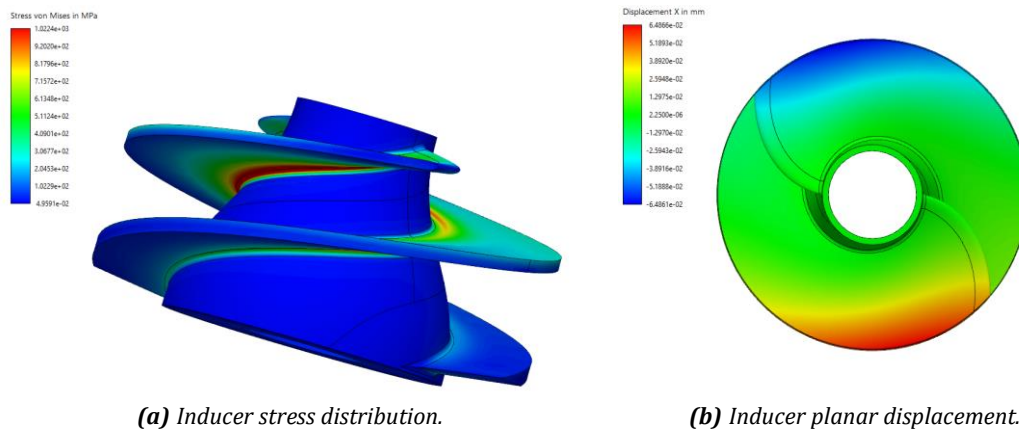


**Figure 39:** Revised inducer structural performance.

Due to increased blade thickness and fillet geometry, the blade root stress was reduced significantly to  $1022\text{MPa}$ . High root stresses were still recorded, and these were linked to an increase in centrifugal load from a higher blade mass. Despite the results not meeting the permissible requirement, the inducer will not experience material failure in the nominal operating case. Horizontal displacement was also reduced to an acceptable level of  $0.0649\text{mm}$ , which does not exceed the tip clearance gap.

### 7.2.3 Revised Dynamic Performance

As a final verification, it was important to check that the new component natural frequencies did not coincide with the pump operating window. The updated frequencies are summarised in Table 14.

**Table 14:** Revised component natural frequencies.

Component	Mode Number	Frequency [Hz]
Inducer	1	8,452
	2	8,454
	3	11,187
	4	11,189
Impeller	1	10,449
	2	11,304
	3	12,703
	4	12,706

Comparison with baseline modal analysis reveals the monitored natural frequencies have all increased. This was due to the use of thicker impeller hub and shroud geometries, and thicker inducer blades, which increased the respective stiffnesses. The level of safety in this aspect of pump operation has, therefore, been improved further.

### 7.2.4 Mass Characteristics

Inducer and impeller mass characteristics were obtained from Autodesk® Inventor for the baseline and optimised configurations. These used the material densities from Table 6 and Table 13, respectively. Component moment of inertia was obtained to provide a relative comparison of how respective spool-up response might vary. Tabulated values are given in Table 15.

**Table 15:** Comparison of baseline and optimised component mass characteristics.

Revision	Component	Mass [g]	Moment of Inertia [gmm <sup>2</sup> ]
Baseline	Inducer	12.5	590
	Impeller	57.0	17,550
Optimised	Inducer	11.9	602
	Impeller	61.8	18,870

Following optimisation, inducer mass decreased by 4.8% and inducer inertia increased by only 1.9%. This was deemed a success. However, due to the implementation of splitter blades and thicker geometries, impeller mass and inertia increased by 8.4% and 7.5%, respectively. This highlights an area for improvement.

## 8.0 Proposed Compressor Prototype

### 8.1 Inducer

The final inducer characteristics are summarised in Table 16. For more detailed dimensions, see Appendix B.

**Table 16:** Final inducer characteristics.

Parameter	Value	Unit
Inlet Hub-Shroud Ratio	0.32	-
Outlet Hub-Shroud Ratio	0.64	-
Shroud Diameter	25.0	mm
Blade Count	2	-
Flow Coefficient	0.110	-
Work Coefficient	0.222	-
Specific Speed	0.970	-
Specific Diameter	2.083	-
NPSHR Estimate	157.3	m
Total Pressure Rise	24.8	bar
Energy Fraction	4.72	%
Axial Thrust	789	N

Mid-span inducer blade angles are given in Table 17.

**Table 17:** Inducer blade angles.

Blade Angle	Value [deg.]
Inlet Blade Angles, $\beta_{b1}$	-77.9
Outlet Blade Angles, $\beta_{b2}$	-71.7

The corresponding inducer mid-span velocity triangles, generated from the 1D model outputs, are shown in Figure 40.

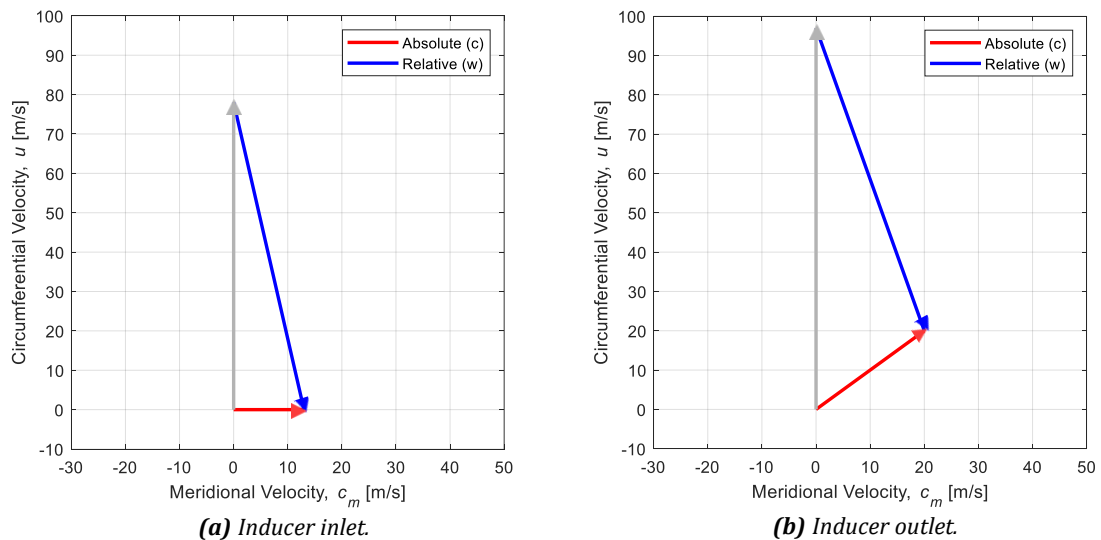


**Figure 40:** Inducer velocity triangles as derived from the 1D model.

## 8.2 Impeller

The final impeller characteristics are summarised in Table 18. For more detailed dimensions, see Appendix C.

**Table 18:** Final impeller characteristics.

Parameter	Value	Unit
Outlet Diameter	55	mm
Outlet Width	3	mm
Diameter Ratio	0.378	-
Outlet Width Ratio	0.063	-
Splitter Blade Count	3	-
Main Blade Count	3	-
Flow Coefficient	0.010	-
Work Coefficient	0.766	-
Specific Speed	0.12	-
Specific Diameter	9.711	-
Total Pressure Rise	501	bar
Energy Fraction	95.3	%

Mid-span impeller blade angles are tabulated in Table 19.

**Table 19:** Impeller blade angles.

Blade Angle	Value [deg.]
Inlet Blade Angles, $\beta_{b3}$	-71.9
Outlet Blade Angles, $\beta_{b4}$	-80.0

The corresponding inducer mid-span velocity triangles are shown in Figure 41.

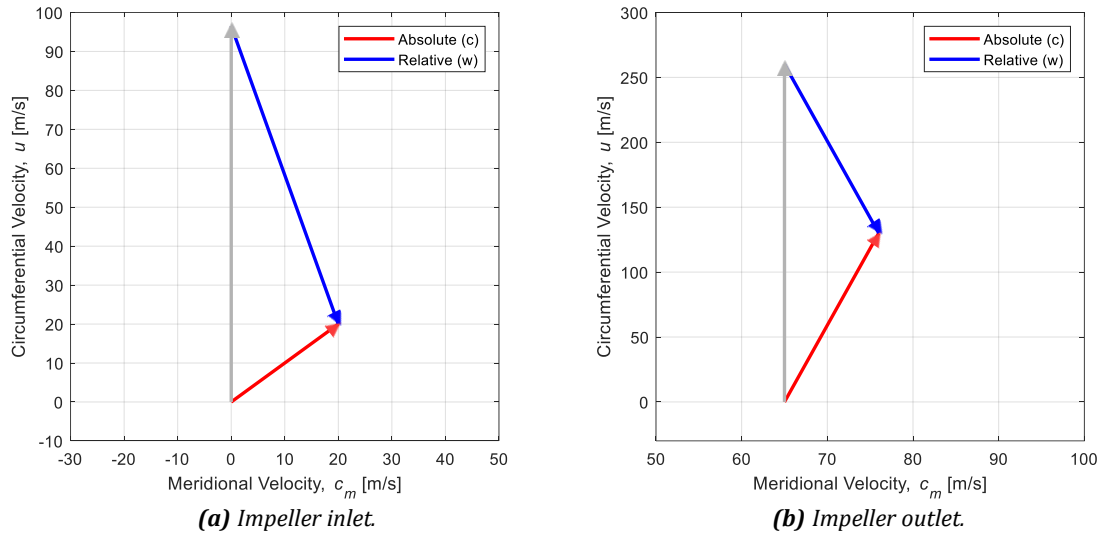
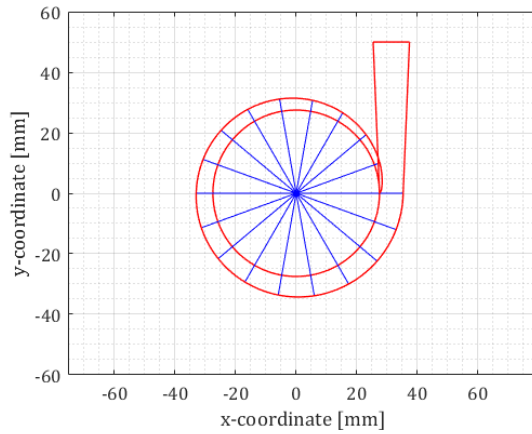


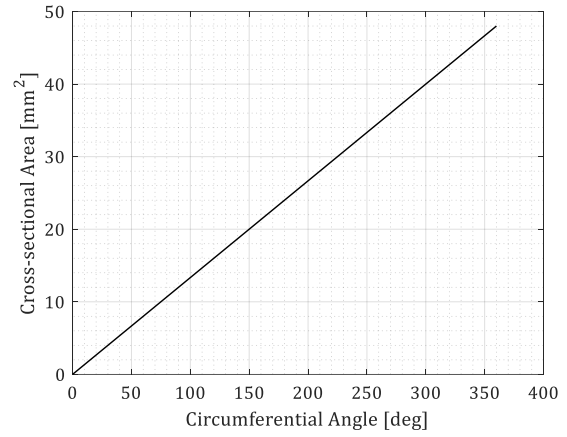
**Figure 41:** Impeller velocity triangles as derived from the 1D model.

### 8.3 Volute

The volute geometry is presented as a spiral contour plot, as shown in Figure 42a. The 1D model gave an exit diameter of  $7.20\text{mm}$  for an inner volute radius of  $32.0\text{mm}$ . The linear variation of cross-sectional area with circumferential angle is shown in Figure 42b.



**(a)** Volute spiral contour.



**(b)** CS area variation with circumferential angle.

**Figure 42:** Design summary of the volute, derived from outputs of the 1D model.



## 9.0 Conclusions and Recommendations

### 9.1 Conclusions

The aim of this project was to conduct the design and optimisation of an HTP turbopump oxidiser compressor. Ultimately, a high pressure, high efficiency, lightweight and compact prototype has been devised. All critical design requirements have been proven to be attainable with slight adjustment to the operating conditions. The implementation of splitter blades, not previously covered for HTP turbopump systems by modern literature, has been successfully explored. The major research outcomes are summarised as follows:

1. The iterative methodology framework was successfully validated through comparison of calculated power requirements from the baseline CFD and 1D model results. The marginal difference was attributed to the exclusion of additional hydraulic efficiencies and viscous effects in the 1D model.
2. Flow performance of the baseline model demonstrated a total pressure rise of 512 *bar* at 90,000 *rpm* and 8.00 *kg/s*. This exceeded the design requirement by an unacceptable level. However, the pump performance map highlighted a mode of operation which aligns with the PU requirements of 360 *bar*, defined as 75,000 *rpm* and 6.00 *kg/s*. This mode improved inducer performance, and reduced component stress and power requirements.
3. Splitter blades were shown to improve the efficiency and reduce streamline deviation within impeller channels at an optimum LE meridional position. The relationship between the efficiency and LE meridional position was confirmed. An optimum 1.6% efficiency increase was recorded at a LE position of 30% meridional length. This formed the basis of an optimised impeller configuration.
4. Structural optimisation was successful in terms of improving load bearing and dynamic characteristics. Increasing blade and hub/shroud thicknesses improved the baseline design, which initially exhibited total material failure. For a permissible stress of 995 *MPa*, the impeller design was accepted. The inducer, however, exceeded this, but still fell below the true material yield strength, and would operate sufficiently. Modal analysis results raised no concerns of resonance. Finally, inducer mass optimisation was successful, with an improvement in structural efficiency of 4.8%.

### 9.2 Recommendations for Future Work

Although the overarching aim and objectives have been met, three key areas of future work, which were outside the scope of this project, were highlighted. These are presented below:

1. **Cavitation performance** was not quantified fully during this study, with regions of low pressure only compared at the impeller inlet. Further work should incorporate a cavitation model, which utilises a fluid with H<sub>2</sub>O and H<sub>2</sub>O<sub>2</sub> mass fractions specified.
2. **Blade mean line design** was outside the scope of the design methodology, given the complicated procedures and reliance on designer experience. Mean line optimisation studies should be conducted to improve overall efficiency and flow quality.
3. **Mapped blade pressure distributions** should be investigated to improve the accuracy of the FEA blade loading. This will offer more insight into structural optimisation due to less conservative stress values.



## 10.0 References

### 10.1 Literature

- [1] Torre F. Design Optimization of Splitter Blades for Rocket Engine Turbopump. ASME 2018 Turbo Expo Turbomachinery Technical Conference & Exposition. 2018.
- [2] Tang H. ME40346: Spacecraft Engineering. Spacecraft Propulsion. Bath: University of Bath. 2021.
- [3] Murray W, Steiner M, Neal J, Hunt S. Design and Analysis of a High-Speed, High-Pressure Peroxide/RP-1 Turbopump. 50th AIAA/ASME/SAE/ASEE Joint Propulsion Conference. 2014.
- [4] Stechmann D P, Lim D, Rotella S, Menon S, Nirudhoddi B. Design and Analysis of a High-Performance Hydrogen Peroxide Thrust Chamber Assembly. 50th AIAA/ASME/SAE/ASEE Joint Propulsion Conference. 2014.
- [5] Moon Y, Park C, Jo S, Kwon S. Design specifications of H<sub>2</sub>O<sub>2</sub>/kerosene bipropellant rocket system for space missions. Aerospace Science and Technology. 2014;33(1):118-121.
- [6] Pelin G, Stoica C, Pelin C, Balasa R. High concentration hydrogen peroxide for rocket fuel applications. INCAS BULLETIN. 2020.
- [7] Surmacz P. GREEN ROCKET PROPULSION RESEARCH AND DEVELOPMENT AT THE INSTITUTE OF AVIATION: PROBLEMS AND PERSPECTIVES. Journal of KONES Powertrain and Transport. 2016;23(1):337-344.
- [8] Krishnan S. Hydrogen Peroxide / Kerosene , Liquid-Oxygen / Kerosene , and Liquid-Oxygen / Liquid Methane for Upper Stage Propulsion. Malaysia: Universiti Teknologi. 2010.
- [9] Sutton G, Biblarz O. Rocket propulsion elements. New York: John Wiley & Sons; 2000.
- [10] Cervone A, Torre L, d'Agostino L, Musker A, Roberts G, Bramanti C, Saccoccia G. Development of Hydrogen Peroxide Monopropellant Rockets. 2006.
- [11] Clark J. Ignition - An Informal History of Liquid Rocket Propellants, Rutgers University Press, New Brunswick, 1972.
- [12] Musker A.J, Rusek J, Kappenstein C, Roberts G. Hydrogen Peroxide—from Bridesmaid to Bride. 3rd ESA International conference on Green Propellants for Space Propulsion. France. 2006.
- [13] Jeff M. Hydrogen Peroxide - The Safe Supply and Handling of HTP. Houston: Solvay Interlox, Inc. 2008.
- [14] Cong Y, Zhang T, Li T, Sun J, Wang X, Ma L, Liang D, Lin L. Propulsive Performance of Hypergolic H<sub>2</sub>O<sub>2</sub>/Kerosene Bipropellant. Journal of Propulsion and Power, 20, 83-86. 2004.
- [15] Pourpoint T, Bland R.A, Meyer S, Heister S, Anderson W. Experimental and Theoretical Performance of High-Pressure Hydrogen Peroxide Catalyst Beds. Journal of Propulsion and Power, 28, 912-917. 2012.
- [16] Ventura M, Wernimont E, Dillard J. Hydrogen Peroxide - Optimal for Turbomachinery and Power Applications. 2007.
- [17] Abdou E, Carvalhar A, Klein M, Otto S, White, R, Harry J, Juangphanich P, McGuire B, Olsavsky S, De Maesschalck C, Pourpoint T. Turbopump Design, Build, and Testing at Purdue University. 55th AIAA Aerospace Sciences Meeting. 2017.
- [18] Chen S. Turbopump Design and Analysis Approach for Nuclear Thermal Rockets. AIP Conference Proceedings. 2006.
- [19] Nourbakhsh A. Turbopumps and pumping systems. Berlin: Springer. 2011.
- [20] Jakobsen J K, Keller R B. Liquid rocket engine turbopump inducers. NASA SPACE VEHICLE DESIGN CRITERIA (CHEMICAL PROPULSION) – NASA SP-8052. Ohio: Cleveland. 1971.
- [21] Liquid rocket engine centrifugal flow turbopumps. NASA SPACE VEHICLE DESIGN CRITERIA (CHEMICAL PROPULSION) – NASA SP-8109. MACHINE ELEMENTS AND PROCESSES. Ohio: Cleveland. 1973.

- [22] Csomor A, Sutton R. Small, high-pressure liquid hydrogen turbopump. Rocketdyne Division – NASA CR-135186. Ohio: Cleveland. 1977.
- [23] Brennen C. Hydrodynamics of Pumps. Oxford: Concepts ETI Inc. and Oxford University Press. 1994.
- [24] Choi C. Numerical Studies on the Inducer/Impeller Interaction Liquid Rocket Engine Turbopump. Journal of Fluid Machinery, 6, 50-57. 2003.
- [25] Hong S-S, Kim D-J, Kim J-S, Choi C-H, Kim J. Study on inducer and impeller of a centrifugal pump for a rocket engine turbopump. Proceedings of the Institution of Mechanical Engineers, Part C: Journal of Mechanical Engineering Science, 227, 311-319. 2013.
- [26] Japikse D. OVERVIEW OF INDUSTRIAL AND ROCKET TURBOPUMP INDUCER DESIGN. Concepts NREC. CAV. 2001.
- [27] Mohr M. A Design Procedure for Low and High Head Inducers. Kaiserslautern: Technical University of Kaiserslautern. 2020.
- [28] Gravdahl J, Egeland O. Centrifugal compressor surge and speed control. IEEE Transactions on Control Systems Technology, 7(5), 567-579. 1999.
- [29] Mentzos M, Filios A, Margaritis D, Papanikas D. CFD predictions of flow through a centrifugal pump impeller. 2005.
- [30] Prasad A S, Lakshmipathi R, Babji A, Babu P K. Static and Dynamic Analysis of a Centrifugal Pump Impeller. International Journal of Scientific & Engineering Research, 4(10), 966-971. 2013.
- [31] Japikse D, Marscher W D, Furst R B. Centrifugal Pump Design and Performance. White River Junction, Vermont: Concepts NREC, 2006.
- [32] Furst R B. Liquid rocket engine centrifugal flow turbopumps. NASA SP-8109, NTIS N74-28961, 1973.
- [33] Torre F, Konno S, Lettieri C, Pini M, Kawata Y. Design Optimization of Splitter Blades for Rocket Engine Turbopump. Volume 2D: Turbomachinery. 2018.
- [34] CFturbo: User manual for CFturbo software. CFturbo GmbH. Unterer Kreuzweg, Germany. 2021.
- [35] Jones C W. Applications of Hydrogen Peroxide and Derivatives - Physical Properties of Hydrogen Peroxide. Royal Society of Chemistry. 1999.
- [36] Constantine M T, Cain E F. Hydrogen Peroxide Handbook. ROCKETDYNE. Canoga Park, California. 1967.
- [37] Ansys, Inc. ANSYS Release 14.0. ANSYS CFX-Solver Modelling Guide. Canonsburg, PA: Ansys, Inc. 2011.
- [38] Noh J-G, Lee E-S, K J, Lee D-S. CFD Analysis of a Partial Admission Turbine Using a Frozen Rotor Method. Proceedings of the Korean Society of Propulsion Engineers Conference. 2004.
- [39] Carnevale M. ME40054: CFD. Practical Lecture. 2: Meshing. Bath: University of Bath. 2021.
- [40] Bathe K-J. Finite element procedures. Watertown, Mass: Prentice-Hall. 2016.
- [41] Brown A M, DeLessio J L. Test-Analysis Modal Correlation of Rocket Engine Structures in Liquid Hydrogen – Phase II. Conference and Exposition on Structural Dynamics: It's Not Just Model Anymore. Orlando, Florida. 2020.
- [42] Hashemi S, Richard M. Natural frequencies of rotating uniform beams with Coriolis effects. Journal of vibration and acoustics, 123(4), 444–455. 2001.
- [43] Patil P M, Todkar R G. An Overview of Effect of Splitter Blades on Centrifugal Pump Performance. International Journal of Engineering Research & Technology (IJERT), 2(11), 2249-2252. 2013.

## 10.2 Figures

- [A] Surmacz P. GREEN ROCKET PROPULSION RESEARCH AND DEVELOPMENT AT THE INSTITUTE OF AVIATION: PROBLEMS AND PERSPECTIVES. *Journal of KONES Powertrain and Transport*. 2016;23(1):337-344.
- [B] U.S. Space & Rocket Center. 2022. *Archives*. [online] Available at: <https://www.rocketcenter.com/archives>. [Accessed 21 April 2022].
- [C] Haidn O. Advanced Rocket Engines. *Advances in Propulsion Technology for High-Speed Aircraft*. 2007.
- [D] Gilmour A. ME40321. Design and Optimisation of a Hydrogen Peroxide Turbopump Compressor. Bath: University of Bath. 2022.
- [E] Chen F, Bi H, Ahn S-H, Zhongyu M, Luo Y, Wang Z. Investigation on Dynamic Stresses of Pump-Turbine Runner during Start Up in Turbine Mode. *Processes*, 9(3), 499. 2021.
- [F] Gilmour A. ME40321. PROJECT PLAN AND LITERATURE REVIEW: Design and Optimisation of a Turbopump Compressor. Bath: University of Bath. 2022.
- [G] Gravdahl J, Egeland O. Centrifugal compressor surge and speed control. *Control Systems Technology, IEEE Transactions on*, 7(5), 567 - 579. 1999.

## 11.0 Appendices

### 11.1 Appendix A – 1D Model Code

CompDesign.m

```
N = 90000; % Shaft Speed [revs/min]
m = 8; % [kg/s]
rho = 1400; % [kg/m^3]
Q = m / rho; % [m^3/s]

deltaP0 = 360 * 10^5; % Total Pressure Rise across compressor / Pa
Ef_inducer = 0.06; % Inducer Energy Fraction
Ef_impeller = 1 - Ef_inducer; % Impeller Energy Fraction

eta_impeller = 0.6; % Impeller preliminary efficiency
eta_inducer = 0.75; % Inducer preliminary efficiency

%% Inducer %%

deltaP0_ind = deltaP0 * Ef_inducer; % Inducer Pressure Rise [Pa]
P_inducer = ((m/rho) * deltaP0_ind) / eta_inducer; % Inducer Power Input [W]

Rhs_i = 0.32; % Hub-shroud Ratio at inlet [-]
Rhs_o = 0.64; % Hub-shroud Ratio at outlet [-]
Ds_i = 25; % Shroud Diameter at inlet [mm]
Ds_o = 25; % Shroud Diameter at outlet [mm]
Dh_i = Rhs_i * Ds_i; % Hub Diameter at inlet
Dh_o = Rhs_o * Ds_o; % Hub Diameter at outlet

%% Impeller %%

deltaP0_imp = deltaP0 * Ef_impeller; % Impeller Pressure Rise [Pa]
P_impeller = (m/rho) * deltaP0_imp / eta_impeller; % Impeller Power Input [W]
Nb_impeller = 5; % Impeller Blade Count [-]

d2 = 55; % Impeller diameter [mm]
dh = 16; % Hub diameter [mm]
ds = Ds_o; % Suction diameter [mm]
b2 = 3; % Impeller width [mm]

%% Call Functions %%

% Inducer %
[BetaB1_inducer, BetaB2_inducer, Cx2, Ctheta_M2, phi_inducer, psi_inducer,
NPSHA, NPSHR, delta_ind, sigma_ind] = InducerModel(m, rho, deltaP0_ind, Ds_i,
Ds_o, Dh_i, Dh_o, N, P_inducer);

% Impeller %
[BetaB3_impeller, BetaB4_impeller, Ctheta_4, r2, phi_impeller, psi_impeller,
delta_imp, sigma_imp, R_dia, R_width] = ImpellerModel(m, rho, d2, dh, ds, b2, N,
P_impeller, Q, Cx2, Ctheta_M2, Nb_impeller, deltaP0_imp);

% Volute %
[D0] = Volute1D(m, Ctheta_4, r2, rho);
```

## InducerModel.m

```
function [BetaB1_inducer, BetaB2_inducer, Cx2, Ctheta_M2, phi_inducer,
psi_inducer, NPSHA, NPSHR, delta_ind, sigma_ind] = InducerModel(m, rho,
deltaP0_ind, Ds_i, Ds_o, Dh_i, Dh_o, N, P_inducer)
%% Initialise Input Parameters %%

Nrad = N * (pi/30); % Shaft speed [rad/s]

rsh1 = Ds_i/2;
rsh2 = Ds_o/2;
rh1 = Dh_i/2;
rh2 = Dh_o/2;

%% Inlet - Station 1 %%

A_i = pi/4 * (Ds_i^2 - Dh_i^2) * 10^-6; % Inlet Area [m^2]

Cx1 = m / (rho * A_i); % Inlet Axial Velocity [m/s]
Cm1 = Cx1;
Ctheta1 = 0;
Cr1 = 0;

Wx1 = Cx1;
Wm1 = Wx1;
Wr1 = 0;
Alpha1 = 0; % Zero prewhirl for all radial positions

%% Outlet - Station 2 %%

A_o = pi/4*(Ds_o^2 - Dh_o^2) * 10^-6; % Outlet Area [m^2]

Cx2 = m / (rho * A_o);
Cm2 = Cx2;
Cr2 = 0;

Wx2 = Cx2;
Wm2 = Wx2;
Wr2 = 0;

%% Output Angle Space %%

BetaB1_inducer = zeros(3,1); % Create space. BetaB1(1,2,3) = Shroud, Mean, Hub
BetaB2_inducer = zeros(3,1); % Create space. BetaB2(1,2,3) = Shroud, Mean, Hub
Alpha2_inducer = zeros(3,1); % Create space. Alpha2(1,2,3) = Shroud, Mean, Hub

%% Shroud Position %%
    %% Inlet %%

    Ush1 = Nrad * rsh1 * 10^-3; % Inlet Shroud Tangential Velocity [m/s]
    Wtheta_sh1 = -1 * Ush1;
    BetaB1_inducer(1) = atan(Wtheta_sh1/Wm1) * 180/pi; % Inlet Shroud Blade
Angle / deg

    %% Outlet %%

    Ush2 = Nrad * rsh2 * 10^-3; % Outlet Shroud Tangential Velocity [m/s]
    Ctheta_sh2 = P_inducer / (m*Ush2);
    Wtheta_sh2 = Ctheta_sh2 - Ush2;
    Alpha2_inducer(1) = atan(Ctheta_sh2/Cm2) * 180/pi;
    BetaB2_inducer(1) = atan(Wtheta_sh2/Wm2) * 180/pi;

%% Area Mean Position %%
rM1 = (rh1 + rsh1)/2; % Area mean radius / mm
rM2 = (rh2 + rsh2)/2; % Area mean radius / mm
    %% Inlet %%

    UM1 = Nrad * rM1 * 10^-3; % Inlet Mean line Tangential Velocity [m/s]
    Wtheta_M1 = -1 * UM1;
    BetaB1_inducer(2) = atan(Wtheta_M1/Wm1) * 180/pi; % Inlet Mean line Blade
Angle [deg]
```

```

%% Outlet %%

UM2 = Nrad * rM2 * 10^-3; % Outlet Mean line Tangential Velocity [m/s]
Ctheta_M2 = P_inducer / (m*UM2);
Wtheta_M2 = Ctheta_M2 - UM2;
Alpha2_inducer(2) = atan(Ctheta_M2/Cm2) * 180/pi;
BetaB2_inducer(2) = atan(Wtheta_M2/Wm2) * 180/pi;

%% Hub Position %%
%% Inlet %%

Uh1 = Nrad * rh1 * 10^-3; % Inlet Hub Tangential Velocity [m/s]
Wtheta_h1 = -1 * Uh1; % Inlet Hub Relative Velocity [m/s]
BetaB1_inducer(3) = atan(Wtheta_h1/Wm1) * 180/pi; % Inlet Shroud Blade Angle
[deg]

%% Outlet %%

Uh2 = Nrad * rh2 * 10^-3; % Outlet Hub Tangential Velocity [m/s]
Ctheta_h2 = P_inducer / (m*Uh2);
Wtheta_h2 = Ctheta_h2 - Uh2;
Alpha2_inducer(3) = atan(Ctheta_h2/Cm2) * 180/pi;
BetaB2_inducer(3) = atan(Wtheta_h2/Wm2) * 180/pi;

%% CFTurbo Design Parameters %%

Pi = 4.15*10^5; % Inlet Stagnation Pressure [Pa]
Pv = 433.6; % HTP Vapour Pressure [Pa]
g = 9.81; % Gravitational Constant [m/s^2]
lambaC = 1.15; % Weighted Parameter (Absolute) [-]
lambaW = 0.2; % Weighted Parameter (Relative) [-]

phi_inducer = Cm1/Ush1; % Flow Coefficient [-]
psi_inducer = deltaP0_ind/(rho*Ush1^2); % Work Coefficient [-]

NPSHA = ((Pi/(rho*g)) + (Cx1^2/(2*g)))-(Pv/(rho*g)); % Available Net Positive
Suction Head [m]
NPSHR = lambaC*(Cx1^2/(2*g)) + lambaW*(Wx1^2/(2*g)); % Required Net Positive
Suction Head [m]

delta_ind = psi_inducer^0.25/phi_inducer^0.5; % Specific Diameter [-]
sigma_ind = phi_inducer^0.5/psi_inducer^0.75; % Specific Speed [-]

end

```

## ImpellerModel.m

```
function [BetaB3_impeller, BetaB4_impeller, Ctheta_4, r2, phi_impeller,
psi_impeller, delta_imp, sigma_imp, R_dia, R_width] = ImpellerModel(m, rho, d2,
dh, ds, b2, N, P_impeller, Q, Cx2, Ctheta_M2, Nb_impeller, deltaP0_imp)
%% Initialise Input Parameters %%

Nrad = N * (pi/30); % Shaft speed [rad/s]

r2 = d2 / 2;
rh = dh / 2;
rs = ds / 2;
%% Inlet - Station 3 %%

Cx3 = Cx2;
Cr3 = 0;
Cm3 = Cx3;
Ctheta_3 = Ctheta_M2;

Wx3 = Cx3;
Wr3 = 0;
Wm3 = Wx3;
%% Outlet - Station 4 %%

A_o = pi * d2 * b2 * 10^-6; % Outlet Area [m^2]

Cx4 = 0;
Cr4 = m / (rho * A_o);
Cm4 = Cr4;

Wx4 = 0;
Wr4 = Cr4;
Wm4 = Wr4;
%% Required Blade Angles %%

BetaB3_impeller = zeros(3,1); % Create space. BetaB1(1,2,3) = Shroud, Mean, Hub
BetaB4_impeller = zeros(1); % Create space.
Alpha3_impeller = zeros(3,1); % Create space. Alpha3(1,2,3) = Shroud, Mean, Hub

%% Inlet Position %%
    %% Shroud Position %%

    Ush3 = Nrad * rs * 10^-3; % Inlet Shroud Tangential Velocity [m/s]
    Ctheta_sh3 = Ctheta_3;
    Wtheta_sh3 = Ctheta_sh3 - Ush3;
    Alpha3_impeller(1) = atan(Ctheta_sh3/Cm3) * 180/pi;
    BetaB3_impeller(1) = atan(Wtheta_sh3/Wm3) * 180/pi; % Inlet Shroud Blade
Angle / deg

    %% Area Mean Position %%

    rM3 = (rh + rs)/2; % Area mean radius [mm]
    UM3 = Nrad * rM3 * 10^-3; % Outlet Mean line Tangential Velocity [m/s]
    Ctheta_M3 = Ctheta_3;
    Wtheta_M3 = Ctheta_M3 - UM3;
    Alpha3_impeller(2) = atan(Ctheta_M3/Cm3) * 180/pi;
    BetaB3_impeller(2) = atan(Wtheta_M3/Wm3) * 180/pi;

    %% Hub Position %%

    Uh3 = Nrad * rh * 10^-3; % Outlet Hub Tangential Velocity [m/s]
    Ctheta_h3 = Ctheta_3;
    Wtheta_h3 = Ctheta_h3 - Uh3;
    Alpha3_impeller(3) = atan(Ctheta_h3/Cm3) * 180/pi;
    BetaB3_impeller(3) = atan(Wtheta_h3/Wm3) * 180/pi;

%% Outlet Position %%

U4 = Nrad * r2 * 10^-3; % Outlet Tangential Velocity [m/s]
Ctheta_4 = ((P_impeller/m) + (Ctheta_M3*UM3))/U4;
Wtheta_4 = Ctheta_4 - U4;
```

```

alpha_h2 = atan(Ctheta_h3/Cm4) * 180/pi;
BetaB4_impeller(1) = atan(Wtheta_4/Wm4) * 180/pi;

sigma = 1 - ((cos(BetaB4_impeller*pi/180))^1/2)/(Nb_impeller^0.7); % Wiesner
Slip Factor
Cslip = (1 - sigma) * U4;

y = Wtheta_4 - Cslip;
BetaB4_test = atan(y/Wm4) * 180/pi;

%% CFTurbo Design Parameters %%

phi_impeller = Cm3/Ush3; % Flow Coefficient [-]
psi_impeller = deltaP0_imp/(rho*U4^2); % Work Coefficient [-]

delta_imp = psi_impeller^0.25/phi_impeller^0.5; % Specific Diameter [-]
sigma_imp = phi_impeller^0.5/psi_impeller^0.75; % Specific Speed [-]

R_dia = ((dh+d2)/2)/d2; % Diameter Ratio [-]
R_width = b2/d2; % Outlet Width Ratio [-]

end

```



## VoluteModel.m

```
function [D0] = VoluteModel(m, Ctheta_4, r2, rho)
%% Establish volute shape based on outlet velocity requirements

r0 = 32; % Outlet Radius [mm]
V0 = (Ctheta_4 * r2) / r0; % Outlet Velocity [m/s]

A0 = (m / (rho * V0))*10^6; % Outlet Area [mm^2]
D0 = ((4 * A0) / pi)^0.5; % Outlet Diameter [mm]

%% Plot Cross-sectional Variation with Circumferential Angle %%
figure(1)
Area = [0;A0];
Angle = [0;360];

plot(Angle,Area,'color','k','linewidth',1)
ylabel('Cross-sectional Area [mm^{2}]')
xlabel('Circumferential Angle [deg]')
set(gca,'fontname','cambria')
set(gca,'FontSize',13)
grid on
grid minor

%% Plot Volute Spiral Contour

figure(2)
th = 0:pi/300:2*pi;
thdeg = th * 180/pi;
xunit = r2 * cos(th);
yunit = r2 * sin(th);
plot(xunit, yunit,'color','r','linewidth',1);
grid on
grid minor
ylabel('y-coordinate [mm]')
xlabel('x-coordinate [mm]')
set(gca,'fontname','cambria')
set(gca,'FontSize',13)
axis equal
hold on

rS = r2 + sqrt(4*(A0/(360*pi))*thdeg);

for iy = 1:length(rS) % Plot Spiral
xunitSpiral(iy) = rS(iy)*cos(th(iy));
yunitSpiral(iy) = rS(iy)*sin(th(iy));
plot(xunitSpiral, yunitSpiral,'color','r','linewidth',1);
iy = iy +1;

end

thetaSpiralDashDeg = [20:20:360]; % 20 degree division markers
thetaSpiralDash = thetaSpiralDashDeg * pi/180;
rSDash = r2 + sqrt((8/(15*pi))*thetaSpiralDashDeg);

for iyD = 1:length(rSDash) % Plot division markers

xunitSpiralDash(iyD) = rSDash(iyD)*cos(thetaSpiralDash(iyD));
yunitSpiralDash(iyD) = rSDash(iyD)*sin(thetaSpiralDash(iyD));

plot([0 xunitSpiralDash(iyD)], [0
yunitSpiralDash(iyD)], 'color','b','linewidth',0.1)

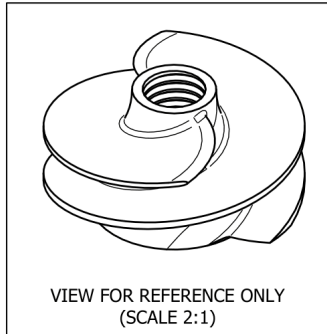
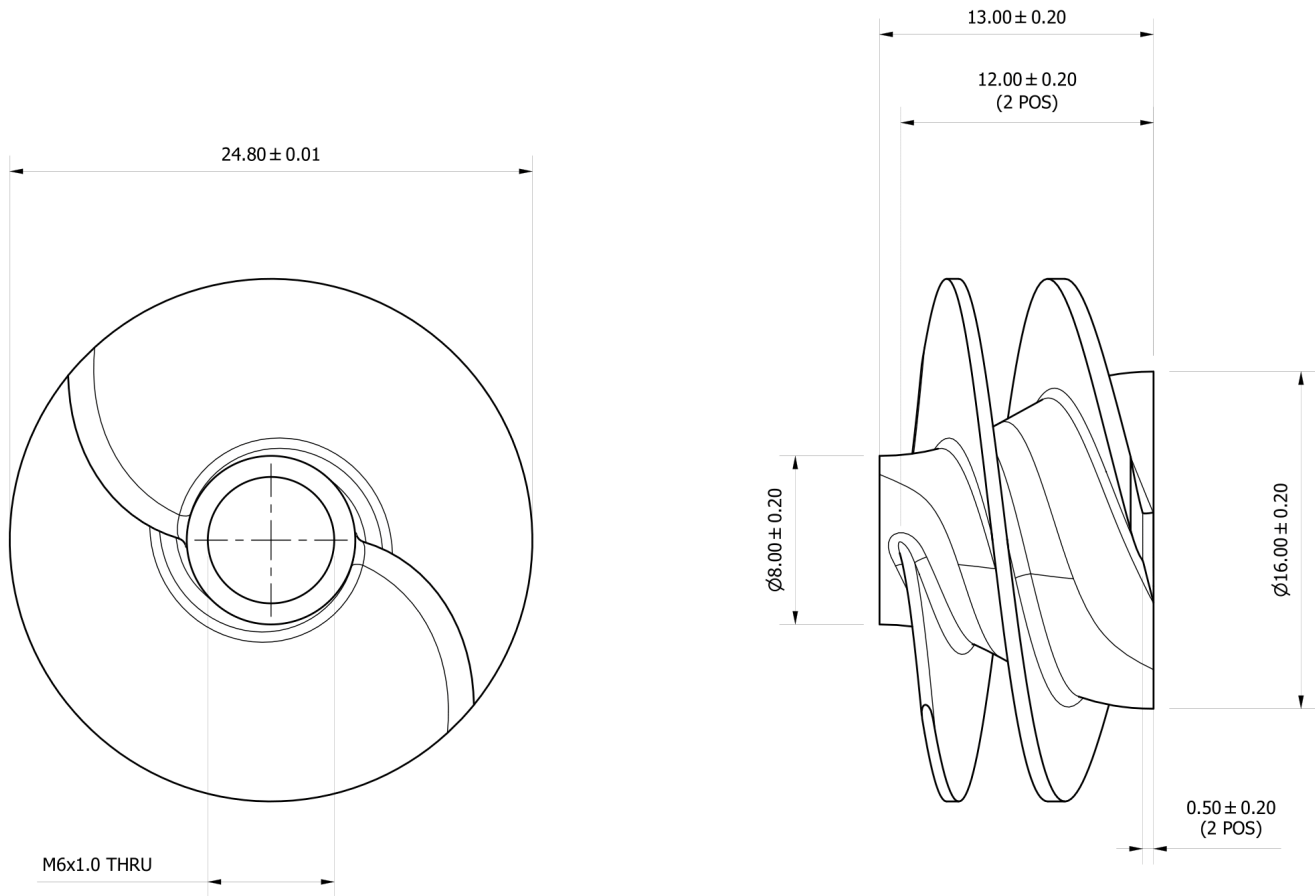
iyD = iyD +1;



end

hold off
```

- NOTES:**
1. MATERIAL SPECIFICATION: SS (17-4 PH GRADE)
  2. FOR ALL UNSPECIFIED DIMENSIONS, CAD MODEL IS MASTER

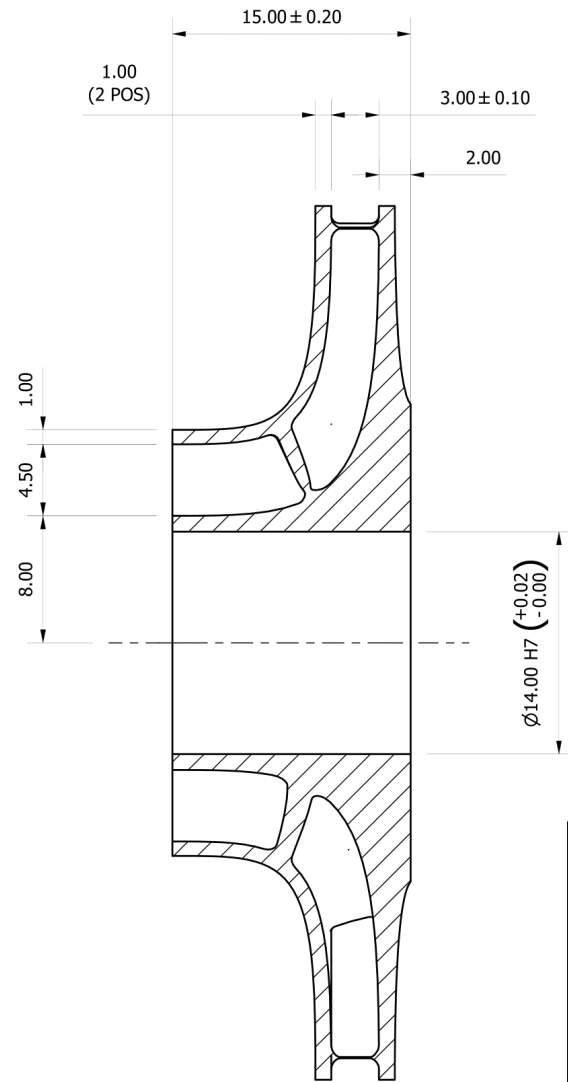
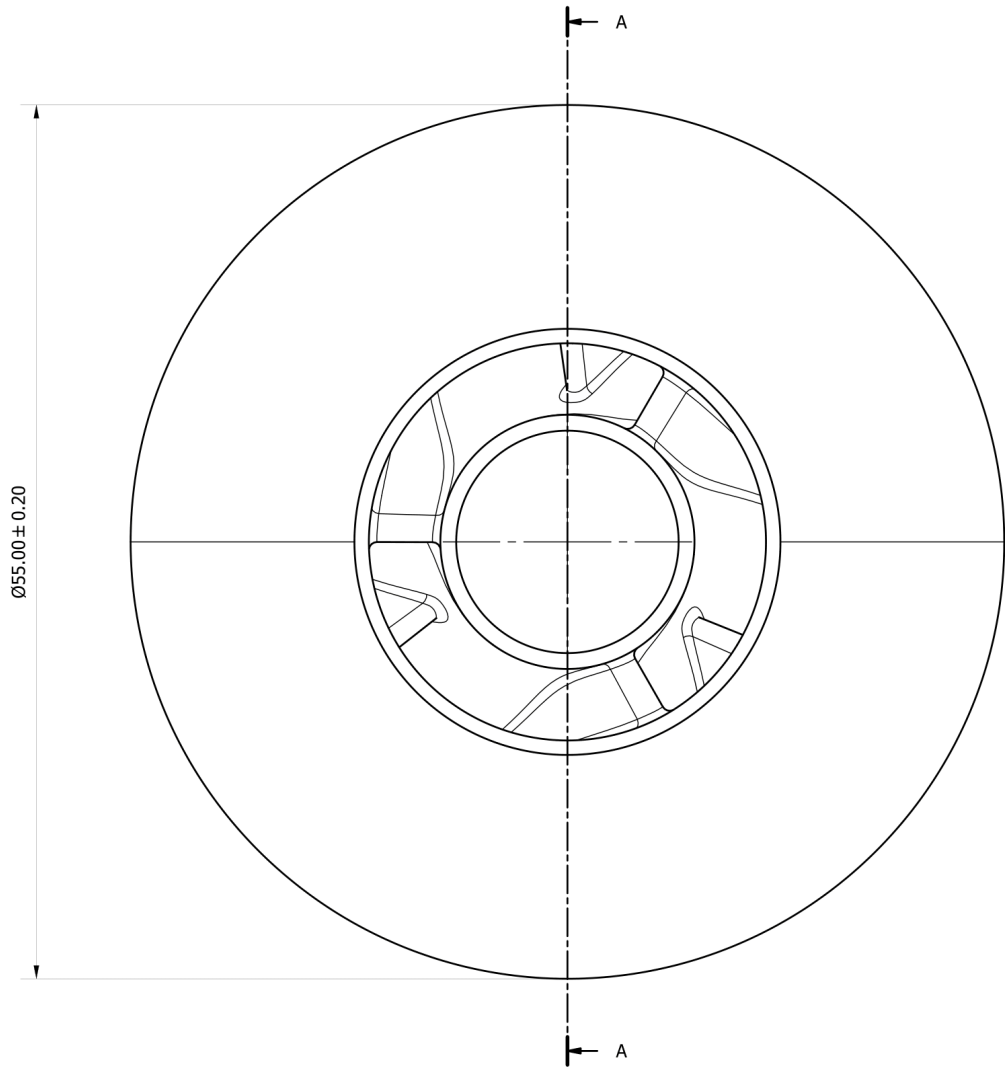
**Appendix B - Impeller Technical Drawing**



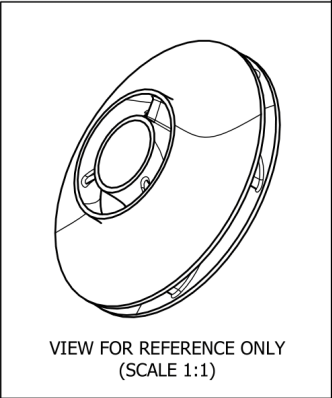
DO NOT SCALE: IF IN DOUBT, PLEASE ASK.		TOLERANCES UNLESS OTHERWISE STATED: ±0.25MM								
ALL DIMS. IN MM SCALE: 4:1	Contact Details: ajg73@bath.ac.uk	Remove all sharpedges. Ro. 0,8 unless stated	Designed by AJG	Checked by H.TANG	Approved by M.CARNEVALE	Sheet size A3	Date 04/05/2022	PROJECT HTP-TP		
 THIRD ANGLE PROJECTION		© UNIVERSITY OF BATH THIS DOCUMENT IS COPYRIGHT AND THE PROPERTY OF THE UNIVERSITY OF BATH. IT MUST NOT BE COPIED IN WHOLE OR IN PART NOR DISCLOSED TO ANY THIRD PARTY WITHOUT PRIOR PERMISSION OF THE UNIVERSITY			Department of Mechanical Engineering		 UNIVERSITY OF BATH		TITLE: HTP TP INDUCER	
						PART No. HTP-P-002	Edition r1	Sheet 1 / 1		

- NOTES:**
- MATERIAL SPECIFICATION: SS (17-4 PH GRADE)
  - FOR ALL UNSPECIFIED DIMENSIONS, CAD MODEL IS MASTER

**Appendix C – Impeller Technical Drawing**

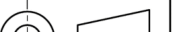



A-A (3:1)



VIEW FOR REFERENCE ONLY  
(SCALE 1:1)

BLADE ANGLE SPEC	
Blade Angle	Value [deg.]
BetaB3	-71.9
BetaB4	-80.0

DO NOT SCALE: IF IN DOUBT, PLEASE ASK.		TOLERANCES UNLESS OTHERWISE STATED: ±0.25MM							
ALL DIMS. IN MM SCALE: 3:1	Contact Details: ajg73@bath.ac.uk	Remove all sharpedges. Ro. 0,8 unless stated	Designed by AJG	Checked by H.TANG	Approved by M.CARNEVALE	Sheet size A3	Date 04/05/2022	PROJECT HTP-TP	
 THIRD ANGLE PROJECTION	© UNIVERSITY OF BATH THIS DOCUMENT IS COPYRIGHT AND THE PROPERTY OF THE UNIVERSITY OF BATH. IT MUST NOT BE COPIED IN WHOLE OR IN PART NOR DISCLOSED TO ANY THIRD PARTY WITHOUT PRIOR PERMISSION OF THE UNIVERSITY				Department of Mechanical Engineering  UNIVERSITY OF BATH		TITLE: HTP TP IMPELLER		
							PART No. HTP-P-001		Edition r1